

SELECTIVITY OF ZEOLITE SUPPORTED RHODIUM AND IRIDIUM
CATALYSTS FOR THE HYDROGENATION OF ALKENES AND ALKYNES

by

Aylin Saltuk

B.S., Chemistry, Boğaziçi University, 2018

Submitted to the Institute for Graduate Studies in
Science and Engineering in partial fulfillment of
the requirements for the degree of
Master of Science

Graduate Program in Chemistry

Boğaziçi University

2022

Dedicated to my family...

ACKNOWLEDGEMENTS

Firstly, I would want to express my respect and thanks to my thesis supervisor, Assoc. Prof. Oktay Demircan for being his student. I am grateful to him for sharing his knowledge and experience with me. His directions and efforts have made a huge contribution to the thesis. I would also like to express my respect and thanks to Prof. Viktorya Aviyente, my thesis co-supervisor, for her invaluable scientific guidance, continuous support and patience. Her belief in me and her encouragement to strive for the best kept me motivated throughout my master's degree.

I wish to extend my appreciation to my thesis committee members: Assoc. Prof. Ece Bulak and Assoc. Prof. Alper Uzun. I am thankful to them for their experience, guidance and valuable remarks during the study.

I would also like to express my gratitude to my colleagues in the Computational Chemistry at Bogazici University (CCBU) for their assistance and collaboration during this time. Foremost, I am grateful to Deniz Akgül for her encouragement, support and help from the first day.

Finally, I wish to thank my parents and my siblings for their love, endless support and the understanding they have shown throughout. I dedicate my thesis to my beloved family.

ABSTRACT

SELECTIVITY OF ZEOLITE SUPPORTED RHODIUM AND IRIIDIUM CATALYSTS FOR THE HYDROGENATION OF ALKENES AND ALKYNES

Alkene and alkyne hydrogenation reactions are currently one of the most common industrial procedures for reducing unsaturated organic compounds to a variety of useful chemicals. In the catalytic hydrogenation of alkenes and alkynes under both homogeneous and heterogeneous conditions, several metal-based catalysts have been used. Metals in supported catalysts are usually cationic and chemically bonded to the supports when they are atomically distributed. The study of noble metals in this class is continually expanding, resulting in the discovery of novel catalysts with unique features. In this study, the selectivity of zeolite supported Rh and Ir catalysts for the hydrogenation of alkenes and alkynes is investigated by using Density Functional Theory (DFT). The reaction pathways for the hydrogenation have been modeled to monitor which pathway is energetically more favorable by comparing the activation barriers between the states. The results have shown that ethylene production is selective with zeolite supported $\text{Rh}(\text{C}_2\text{H}_2)_2$ catalyst. Moreover, the ethylene selectivity for the hydrogenation is more favorable when the metal is Ir. However, the regeneration of the catalyst is facile with Rh metal. This outcome is elucidated by analyzing geometric parameters, ligand bond dissociation energies and potential energy surfaces. This study contributes to a better understanding of ethylene selectivity along the hydrogenation of acetylene. This study is expected to shed light on the synthesis and usage of single atom catalysts for the hydrogenation of acetylene and ethylene.

ÖZET

ALKENLERİN VE ALKİNLERİN HİDROJENASYONU İÇİN ZEOLİT DESTEKLİ RODYUM VE İRİDYUM KATALİZÖRLERİNİN SEÇİCİLİĞİ

Alken ve alkin hidrojenasyon reaksiyonları, doymamış organik bileşiklerin çeşitli faydalı kimyasallara indirgenmesi için halen en yaygın endüstriyel yöntemlerden biridir. Alkenlerin ve alkinlerin hem homojen hem de heterojen koşullar altında katalitik hidrojenasyonunda, çeşitli metal bazlı katalizörler kullanılmıştır. Destekli katalizörlerdeki metaller genellikle katyoniktir ve atomik olarak dağıldıklarında desteklere kimyasal olarak bağlanırlar. Bu sınıftaki soy metallerin incelenmesi, benzersiz özelliklere sahip yeni katalizörlerin keşfedilmesiyle sonuçlanmakta ve sürekli genişlemektedir. Bu çalışmada, alken ve alkinlerin hidrojenasyonu için zeolit destekli Rh ve Ir katalizörlerinin seçiciliği, Yoğunluk Fonksiyonel Teorisi (YFT) kullanılarak araştırılmıştır. Hidrojenasyon için reaksiyon yolları, temel konumlar arasındaki aktivasyon bariyerlerinin karşılaştırılarak hangi yolun daha az enerjiye ihtiyaç duyacağı sorgulanmakta ve modellenmektedir. Sonuçlar, etilen üretiminin zeolit destekli $Rh(C_2H_2)_2$ katalizörü ile seçici olduğunu göstermiştir. Ayrıca, hidrojenasyon için etilen seçiciliği, metal Ir olduğunda daha elverişlidir. Bununla birlikte, katalizörün rejenerasyonu Rh metali ile kolaydır. Bu sonuç, geometrik parametreler, ligand bağ ayrışma enerjileri ve potansiyel enerji yüzeyleri değerlendirilerek açıklanmıştır. Bu çalışmanın, asetilenin hidrojenasyonu boyunca etilen seçiciliğinin daha iyi anlaşılmasına katkıda bulunacağı, asetilen ve etilenin hidrojenasyonu için tek atomlu katalizörlerin sentezi ve kullanımına yol gösterici olması beklenmektedir.

TABLE OF CONTENTS

ACKNOWLEDGMENTS.....	iv
ABSTRACT.....	v
ÖZET.....	vi
LIST OF FIGURES.....	ix
LIST OF TABLES.....	xii
LIST OF SYMBOLS.....	xv
LIST OF ACRONYMS/ABBREVIATIONS.....	xvii
1. INTRODUCTION.....	1
1.1. Aim of the Study.....	2
2. METHODOLOGY.....	3
2.1. Density Functional Theory.....	4
2.2. Functionals.....	6
2.3. Basis Sets.....	7
2.4. Population Analysis.....	8
3. LITERATURE BACKGROUND.....	10
3.1. Catalysis.....	10
3.1.1. Single Atom Catalysis.....	11
3.1.2. The Application of Single Atom Catalysts in Selective Hydrogenation.....	12
3.1.2.1. Selective Hydrogenation of Alkynes.....	14

4. RESULTS	15
4.1. Computational Procedure.....	15
4.2. Usage of Zeolite Supported-Rh(C ₂ H ₂) ₂ as a Catalyst.....	16
4.3. Comparison of Zeolite Supported Rh(C ₂ H ₂) ₂ and Ir(C ₂ H ₂) ₂ Catalysts.....	37
4.3.1. Bond Lengths.....	38
4.3.2. Ligand Bond Dissociation Energies.....	40
4.3.3. Potential Energy Surfaces.....	44
4.3.4. Charges on Metal.....	51
5. CONCLUSION.....	53
REFERENCES.....	55
APPENDIX A: COPY-RIGHT LIST.....	70

LIST OF FIGURES

Figure 1.1.	Stepwise hydrogenation reactions of acetylene [15]	1
Figure 3.1.	Diagram of single atom catalysts for various types of selective hydrogenation [85]	13
Figure 3.2.	Hydrogenation mechanism of acetylene to ethane on the PdIn(110)[97].....	14
Figure 4.1.	3D structure (left) and 2D model (right) of the Rh(C ₂ H ₂) ₂ -zeolite complex...	16
Figure 4.2.	2D mechanism for the hydrogenation of acetylene on the zeolite supported Rh complexes (Path 1)	17
Figure 4.3.	Potential energy surface diagram for the acetylene hydrogenation of zeolite supported complexes (Path 1)	22
Figure 4.4.	2D mechanism for the replacement of ethylene with acetylene on the zeolite supported Rh complexes (Path 1A).....	23
Figure 4.5.	Potential energy surface diagram for the regeneration of the catalyst and emission of ethylene (Path 1).....	25
Figure 4.6.	Comparison of the 2D mechanisms of Path 1 for the hydrogenation of acetylene and Path 1A for the regeneration of the catalyst in the zeolite supported Rh complexes.....	26
Figure 4.7.	Potential energy surface diagram of Path 1 and Path 1A	27

Figure 4.8. 2D mechanism for the replacement of acetylene with ethane on the zeolite supported Rh complexes (Path1B).....	27
Figure 4.9. Potential energy surface diagram for the regeneration of the catalyst and emission of ethane (Path1B).....	28
Figure 4.10. 2D mechanism of the hydrogenation of ethylene or acetylene on the zeolite supported Rh complexes.....	29
Figure 4.11. Potential energy surface diagrams for the selectivity of acetylene versus ethylene for Path 1 and Path 2.....	31
Figure 4.12. 2D mechanism for the hydrogenation of ethylene groups on the zeolite supported Rh complexes (Path 2A).....	31
Figure 4.13. Potential energy surface diagram for the ethylene hydrogenation in zeolite supported Rh complexes (Path 2A).....	32
Figure 4.14. 2D mechanism for the replacement of two ethylene groups with acetylene groups on the zeolite supported Rh complexes (Path2B).....	35
Figure 4.15. Potential energy surface diagram for the regeneration of the catalyst and emission of ethylene (Path 2B).....	37
Figure 4.16. Ligand bond dissociation energy for C ₂ H ₂ in the Rh(C ₂ H ₂)(C ₂ H ₄) complex....	42
Figure 4.17. Ligand bond dissociation energy for C ₂ H ₂ in the Ir(C ₂ H ₂)(C ₂ H ₄) complex.....	42
Figure 4.18. Ligand bond dissociation energy for C ₂ H ₄ in the Rh(C ₂ H ₂)(C ₂ H ₄) complex...	43
Figure 4.19. Ligand bond dissociation energy for C ₂ H ₄ in the Ir(C ₂ H ₂)(C ₂ H ₄) complex.....	43

Figure 4.20. Potential energy surface diagram for the acetylene hydrogenation of zeolite supported $\text{Rh}(\text{C}_2\text{H}_2)_2$ and $\text{Ir}(\text{C}_2\text{H}_2)_2$ complexes (Path 1).....	45
Figure 4.21. Potential energy surface diagram for the acetylene hydrogenation of zeolite supported $\text{Rh}(\text{C}_2\text{H}_2)_2$ and $\text{Ir}(\text{C}_2\text{H}_2)_2$ complexes (Path 1).....	46
Figure 4.22. Potential energy surface diagram for the acetylene hydrogenation of zeolite supported $\text{Rh}(\text{C}_2\text{H}_4)_2$ and $\text{Ir}(\text{C}_2\text{H}_4)_2$ complexes (Path 2A).....	47
Figure 4.23. Potential energy surface diagram for the regeneration of zeolite supported $\text{Rh}(\text{C}_2\text{H}_2)(\text{C}_2\text{H}_4)$ and $\text{Ir}(\text{C}_2\text{H}_2)(\text{C}_2\text{H}_4)$ complexes (Path 1A).....	48
Figure 4.24. Potential energy surface diagram for the regeneration of zeolite supported $\text{Rh}(\text{C}_2\text{H}_2)(\text{C}_2\text{H}_6)$ and $\text{Ir}(\text{C}_2\text{H}_2)(\text{C}_2\text{H}_6)$ complexes (Path 1A).....	49
Figure 4.25. Potential energy surface diagram for the acetylene hydrogenation of zeolite supported $\text{Rh}(\text{C}_2\text{H}_2)(\text{C}_2\text{H}_4)$ and $\text{Ir}(\text{C}_2\text{H}_2)(\text{C}_2\text{H}_4)$ complexes (Path 2).....	50
Figure A.1. The license for Figure 1.1.....	70
Figure A.2. The license for Figure 3.1.....	70
Figure A.3. The license for Figure 3.2.....	71

LIST OF TABLES

Table 4.1.	Ground state geometries, bond distances (Å) and CM5 charges of (1-3)	18
Table 4.2.	Ground state geometries, bond distances (Å) and CM5 charges of (4-6)	19
Table 4.3.	Ground state geometries, bond distances (Å) and CM5 charges of (7-9)	20
Table 4.4.	Transition state geometries and bond distances (Å) for Path 1.....	21
Table 4.5.	Ground and transition state geometries and bond distances (Å) for Path 1A..	25
Table 4.6.	Ground and transition state geometries and bond distances (Å) for Path 1B....	28
Table 4.7.	Ground and transition state geometries and bond distances (Å) for Path 2.....	30
Table 4.8.	Ground state geometries and bond distances (Å) for Path 2A.....	33
Table 4.9.	Transition state geometries and bond distances (Å) for Path 2A.....	34
Table 4.10.	Ground and transition state geometries and bond distances (Å) for Path 2B..	36
Table 4.11.	3D geometries of complex 1, 5 and 15 with M-C and M-O bond distances (Å).....	39

Table 4.12. M-C and M-O bond distances (Å) for complexes 1, 5 and 15.....	40
Table 4.13. C-C triple and double bond lengths (Å) for complexes 1, 5 and 15.....	40
Table 4.14. Ligand bond dissociation energies (kcal/mol) of complex 5 for Rh and Ir complexes.....	41
Table 4.15. 2D structures of each complex with relative Gibbs free energies (Path 1)....	45
Table 4.16. 2D structures of each complex with relative Gibbs free energies (Path 1)....	46
Table 4.17. 2D structures of each complex with relative Gibbs free energies (Path 2A)..	47
Table 4.18. 2D structures of each complex with relative Gibbs free energies (Path 1A)..	48
Table 4.19. 2D structures of each complex with relative Gibbs free energies (Path 1B)..	49
Table 4.20. 2D structures of each complex with relative Gibbs free energies (Path 2)....	50
Table 4.21. CM5 charges on metal for the hydrogenation of Rh(C ₂ H ₂) ₂ and Ir(C ₂ H ₂) ₂ complexes (Path1)	51
Table 4.22. CM5 charges on metal for the regeneration of Rh(C ₂ H ₂) ₂ and Ir(C ₂ H ₂) ₂ complexes (Path 1A).....	51

Table 4.23. CM5 charges on metal for the regeneration of Rh(C ₂ H ₂) ₂ and Ir(C ₂ H ₂) ₂ complexes (Path 1B).....	52
--	----

LIST OF SYMBOLS

E_{el}	Electronic Energy
$E_c[\rho]$	Correlation Energy
$E_x[\rho]$	Exchange Energy
\hat{H}	Hamiltonian Operator
h_{KS}	Kohn-Sham Hamiltonian Operator
$J[\rho(\mathbf{r})]$	Coulomb Energy
q_A	Atomic Charge
$T[\rho(\mathbf{r})]$	Kinetic energy of interacting electrons
$T_{ni}[\rho(\mathbf{r})]$	Kinetic energy of non-interacting electrons
$V_{ext}(\mathbf{r})$	External potential
$V_{ee}[\rho(\mathbf{r})]$	Electron-Electron Interactions
V_{KS}	Kohn-Sham potential
V_{OC}	Open circuit potential
V_{XC}	Exchange-correlation potential
Z	Atomic Number
$\rho(\mathbf{r})$	Electron Density
\hbar	Planck's constant
ψ_i	Kohn-Sham Orbitals
ψ	Wavefunction
∇^2	Laplacian operator

LIST OF ACRONYMS/ABBREVIATIONS

B3LYP	Becke-3-Parameter Lee-Yang-Par functional
CM5	Charge Model 5
DFT	Density Functional Theory
GGA	Generalized Gradient Approximation
GTO	Gaussian Type Orbital
HF	Hartree-Fock Theory
HPA	Hirshfeld Population Analysis
LANL2DZ	Los Alamos National Laboratory 2 Double- ζ
LDA	Local Density Approximation
LDE	Ligand Bond Dissociation Energy
M06-2X	Hybrid Meta Exchange-Correlation Functional
NPA	Natural Population Analysis
PBE	Perdew-Burke-Ernzerhof functional
PES	Potential Energy Surface
SAC	Single Atom Catalyst
STO	Slater Type Orbital
TS	Transition State

1. INTRODUCTION

Alkene and alkyne hydrogenation reactions are currently one of the most common industrial procedures for reducing unsaturated organic compounds to a variety of useful chemicals [1-3]. In the catalytic hydrogenation of alkenes and alkynes under both homogeneous and heterogeneous conditions, several metal-based catalysts such as nickel, palladium, ruthenium, rhodium, iridium, and platinum have been used [4-5]. The ability to elucidate the catalytic behavior of transition metal catalyzed homogeneous molecular hydrogenation reactions is currently centered on ligand design obtained so far demonstrate that the coordination environment around the metal atom is the key to control the catalytic behavior of these catalysts. Ligands have important roles for stabilizing metals, so the metal sites in these supports often need ligands [6].

Because they present unique catalytic capabilities and effective use of expensive transition metals, atomically dispersed metal catalysts on supports gain a lot of attention. Despite numerous studies into the structure and performance of metal-oxide supports, little is known about how to modulate their catalytic capabilities [7]. The compositions and structures of metals bound to the supports determine the electron donor characteristics of the supports. Molecules in close near to contact metal centers on surfaces can also behave as ligands [8-10].

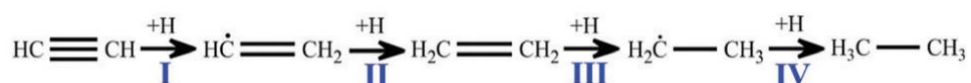


Figure 1.1. Stepwise hydrogenation reactions of acetylene [15].

The selective hydrogenation of alkynes to the corresponding alkenes, i.e., *semihydrogenation*, is an important and challenging type of conversion in synthetic organic chemistry with major practical applications [11].

Because acetylene undergoes two sequential hydrogenation processes, the catalysts used in acetylene semi hydrogenation must be highly selective and must be exceedingly active [12]. Metals such as platinum and palladium, are commonly used as catalysts in these types of processes [13]. However, palladium like catalysts' over hydrogenation of ethylene to ethane remains a major disadvantage, and palladium shortage has inspired renewed research in alternative selective hydrogenation catalysts [14].

Because of their microporous crystalline nature, *zeolites* are a valuable family of catalysts with a wide range of commercial applications [15-21]. Among zeolite-supported catalytic processes, hydrocarbon transformations to create higher alkenes via C-C coupling are quite widespread [22-25]. Alkene hydrogenation and oligomerization processes have been known to be catalyzed by site-isolated Rh(I) complexes anchored on strongly dealuminated zeolite HY (faujasite, FAU) [26-27]. The structural characterization of such catalysts provides great chances for elucidating the reaction mechanisms and the selectivity of the catalytic processes. During the past decade, computational modeling of zeolite and reactions have complemented the experimental studies for a better understanding of the complex reaction mechanisms taking place inside zeolite [28–35].

1.1. Aim of the Study

In this study, hydrogenation reaction mechanism of Rh complexes bonded to zeolite support have been investigated with the aim of understanding the catalytic activity and selectivity. The reaction pathways have been modeled to monitor which pathway is energetically more favorable by comparing the activation barriers between the states. In addition, the modification of the transition metal is examined to indicate the effect of the electronic environment and electron-donor/acceptor properties on metal-oxide supported complex.

The study will include 2 parts:

- i. Usage of zeolite supported-Rh(C₂H₂)₂ as a catalyst
- ii. Comparison of Rh(C₂H₂)₂ and Ir(C₂H₂)₂ catalysts.

2. METHODOLOGY

Quantum chemistry is mainly concerned with the behavior of electrons in the presence of an electromagnetic field generated by nuclear charge. While classical mechanics illustrates systems by specifying velocities and positions, quantum mechanics employs a mathematical vector known as a wavefunction, which theoretically contains all the information about a system. By solving the Schrodinger equation, all the characteristics of this system may be stated as follows:

$$\hat{H} \psi = E \psi. \quad (2.1)$$

\hat{H} denotes the Hamiltonian operator, E is the system's total energy, and ψ corresponds to the wave function. The \hat{H} operator is made up of the kinetic and potential energy terms of nuclei and electrons given as follows:

$$\hat{H} = - \sum_i \frac{\hbar^2}{2m_e} \nabla_i^2 - \sum_k \frac{\hbar^2}{2m_k} \nabla_k^2 - \sum_i \sum_k \frac{e^2 Z_k}{r_{ik}} + \sum_{i < j} \frac{e^2}{r_{ij}} + \sum_{k < l} \frac{e^2 Z_k Z_l}{r_{kl}}, \quad (2.2)$$

where electrons are represented by i and j , nuclei by k and l , and nuclei and electron weights by m_k and m_e , respectively. \hbar stands for “ $h/2\pi$ ” which represents Planck's constant, e is electron charge, Z is atomic number, r is the distance between particles and ∇^2 for the Laplacian operator. The system's energy is expressed by all five components in Equation (2.2). The kinetic energy of electrons and nuclei is given by the first two terms. The potential energies arising from Coulomb interactions of nucleus-electron, electron-electron and nucleus-nucleus are denoted by the other terms.

The Schrödinger equation is correct for small systems such as the hydrogen atom and hydrogen-like ions, but it cannot provide an exact solution for many-particle systems due to particle associative movements. Nuclei are much heavier than electrons, so they appear as a stationary charged point when compared to electrons. Thus, their kinetic energy terms will be zero.

The Born-Oppenheimer (BO) [36] approximation proposes that the motion of the nuclei and electrons of the atom be separated, that the motion of the nuclei be ignored and considered stationary, and that the nucleus-electron attraction be eliminated. In this approach, the Hamiltonian operator becomes

$$H_{el} = E_k^{kin} + U_{ki} + U_{ij} , \quad (2.3)$$

where U_{ki} and U_{ij} are the nucleus-nucleus and electron-electron potential energies, respectively. When this approximation is applied to the Schrödinger equation, it becomes:

$$(H_{el} + V_{nn}) \psi_{el} = E_{el} \psi_{el} , \quad (2.4)$$

where V_{nn} represents the nucleus-nucleus repulsion energy constant, and the E_{el} as an eigenvalue, represents the electronic energy. The variational concept allows the Schrödinger equation to be applied for all other systems. When both sides of Equation (2.1) are multiplied by ψ , the result is

$$\psi H \psi = \psi E \psi. \quad (2.5)$$

Integration of both sides in a volume ($d\tau$) yields the following for many electron systems as follows:

$$E = \frac{\int \psi H \psi d\tau}{\int \psi^2 d\tau} . \quad (2.6)$$

This theorem states that calculated energy (E) can be equal to or greater than ground state energy E_0 . It provides an approximate solution to Schrödinger's equation. This study's methodology is mostly based on density functional theory, which is a variational method. The theory will be explained in detail in the following section.

2.1. Density Functional Theory

Density Functional Theory (DFT) [37], a commonly used quantum chemistry approach, was proposed by Hohenberg and Kohn [38-39] in 1964. This method relies on the Hohenberg-Kohn Existence Theorem [40]. It allows calculating the electrical structure of molecules. According to the theorem, the wavefunction may be computed if the system's ground state density is known. Hohenberg and Kohn also demonstrate that the external potential $V(r)$ is proportional to the electron density $\rho(r)$.

Electron density can be defined as follows:

$$\rho(r): N \int \dots \int |\Psi(r_1, r_2, \dots, r_n)|^2 dr_1 dr_2 \dots dr_n \quad (2.7)$$

The electron density is defined by Equation (2.7), where r_i denotes the electron coordinates. According to the Hohenberg Variational Theorem, when the charge density is in the ground state, the energy content gets its minimal value. The electronic energy of the ground state as a function of electron density becomes

$$E[\rho(r)] = \int V(r)\rho(r)dr + T[\rho(r)] + V_{ee}[\rho(r)], \quad (2.8)$$

where $T[\rho(r)]$ represents the kinetic energy of interacting electrons and $V_{ee}[\rho(r)]$ represents the energy of interelectronic interaction. Equation (2.8) can be reformulated using Kohn and Sham's concept for noninteracting electrons [41], the equation has become

$$E[\rho(r)] = \int V(r)\rho(r)d(r) + T_{ni}[\rho(r)] + J[\rho(r)] + E_{XC}[\rho(r)], \quad (2.9)$$

where $J[\rho]$ and $T_{ni}[\rho]$ denote the Coulomb energy and kinetic energy of noninteracting electrons, respectively and $E_{XC}[\rho]$ represents the exchange-correlation energy functional. The Coulomb energy of electron-electron interactions is written as:

$$E_{XC}[\rho(r)] = \int \rho(r)\epsilon_{XC}(\rho(r))dr. \quad (2.10)$$

By solving the Kohn-Sham equations, the independent orbitals ψ_i also known as Kohn-Sham orbitals, are established as follows:

$$h_i^{KS}\chi_i = \epsilon_i\chi_i. \quad (2.11)$$

The Kohn-Sham Hamiltonian h_i , is described as:

$$h_i^{KS} = -\frac{\nabla^2}{2} - \sum_k^M \frac{Z_k}{|r_i - r_k|} + \int \frac{\rho(r)}{r_{ij}} dr + V_{XC}, \quad (2.12)$$

where V_{XC} denotes the exchange-correlation potential and is proportional to the exchange correlation energy by

$$V_{XC} = \frac{\delta E_{XC}}{\delta \rho}. \quad (2.13)$$

V_{XC} is separated into two: an exchange functional and a correlation functional:

$$E_{XC}[\rho] = E_X[\rho] + E_C[\rho]. \quad (2.14)$$

The correlation term refers to interactions between electrons with opposite spins, whereas the exchange term refers to interactions between electrons with the same spin. It is unknown what the exact form of exchange-correlation energy is.

2.2. Functionals

Because the actual exchange-correlation term is unknown, numerous approximations were devised as DFT progressed to estimate the approximate exchange-correlation term. The first approximation to determine E_{xc} is the Local Density Approximation (LDA). According to this approach, the electron density of a given system is the same in each site, as if it were a uniform gas, and the system becomes neutral when electrostatic energy of positive charge E_b is provided. The energy expression is

$$E[\rho] = T_{ni}[\rho] + \int \rho(r)v(r)dr + J[\rho] + E_{xc}[\rho] + E_b. \quad (2.15)$$

Since the electron density and positive charge density are equal, the equation can be simplified to

$$E[\rho] = T_{ni}[\rho] + E_{xc}[\rho]. \quad (2.16)$$

E_{xc} can be divided into 2 functionals: an exchange functional and a correlation functional:

$$E[\rho] = T_{ni}[\rho] + E_x[\rho] + E_c[\rho], \quad (2.17)$$

where $T_{ni}[\rho]$ is the kinetic energy functional.

$$T_{ni}[\rho] = C_F \int \rho(r)^{5/3} dr. \quad (2.18)$$

C_F is a constant that equals 2.8712. The following equation can be used to calculate the exchange functional.

$$E_x[\rho] = -C_x \int \rho(r)^{4/3} dr. \quad (2.19)$$

The C_x constant is 0.7386. The correlation energy term, $E_c[\rho]$, is obtained by parametrizing the results of a set of quantum Monte Carlo calculations. However, since electron concentrations vary throughout a molecule, it cannot be dispersed uniformly. As a result, LDA is not suitable for determining the exact exchange-correlation functional.

Due to LDA's inadequacies on this topic, the Generalized Gradient Approximation (GGA) [42] approach is developed. The electron density is considered nonhomogeneous by GGA because the exchange and correlation energies are affected by the density gradient. The energy expression is given by

$$E_{XC}^{GGA}[n] = \int dr n(r) \epsilon_{XC}(n(r), |\nabla n(r)|). \quad (2.20)$$

PBE [43] is the most universal GGA and can be used on both molecules and solids, including metals. It is neither the most accurate GGA for tiny organic molecules [44] nor the best for bulk solids lattice characteristics [45]. However, the relevance of being universal is that once a functional works for a specific property/system, it is unavoidably applied more broadly. Organic reactions on metal surfaces, for example, have been extensively investigated, and PBE (or a version) is therefore required to properly treat the bulk metal [46]. Alternative approaches that combine GGA with a proportion of Hartree-Fock (HF) exchange are hybrid density functional methods. The Hartree-Fock (HF) exact exchange is combined with LDA or GGA exchange-correlation functionals to form hybrid functionals. For example, the PBE0 hybrid functional [47] yields the total energy given by

$$E_{XC} = E_{XC}^{PBE} + \frac{1}{4} [E_X^{HF} - E_X^{PBE}], \quad (2.21)$$

where PBE refers to the Perdew-Burke-Ernzerhof GGA exchange-correlation functional.

2.3. Basis Sets

A basis set [48] is a collection of functions used to characterize the orbitals of a system. Linear combinations of atomic orbitals (LCAO) with varying coefficients are used to expand basis functions as follows:

$$\phi_i = \sum_{\mu=1}^K c_{\mu i} f_{\mu} \quad (2.22)$$

where ϕ_i denotes molecular orbitals, f_{μ} atomic orbitals, $c_{\mu i}$ coefficients and K represents the total number of basis functions for atomic orbital functions.

Basis sets are divided into two types: Slater-type orbitals (STOs) and Gaussian-type orbitals (GTOs). Although STO is correct in providing the solution to the Schrödinger equation for hydrogen atoms, it has a significant computational cost. GTOs, on the other hand, are superior to STOs since increasing the number of integrals increases the computational time. S. Francis Boys' [49] GTOs are extensively used basis sets in DFT studies. They are the best approximations to STOs.

Pople et al. developed split-valence basis sets that treat the core and valence orbitals differently. The most well-known are 3-21G, 6-21G, 6-31G*, 6-311G**, and 6-31++G**. The first number represents the number of primitives used for inner shell orbitals, while the numbers after the hyphen represent the number of primitives used for valence orbitals. To get a better approximation to the exact electronic energy, the basis sets can be modified by adding two functions: polarization and diffuse functions. An asterisk (*) at the end of a basis set or (d) indicates the addition of a polarization function for heavy atoms, but a double asterisk ** or (d,p) is used for light atoms such as hydrogen or helium. Furthermore, diffuse functions are denoted by "+," and they allow orbitals to occupy bigger spaces. One plus sign implies that diffuse functions are exclusively added to heavy atoms, whereas "++" indicates that diffuse functions are also added to hydrogen atoms.

2.4. Population Analysis

Since there is no quantum mechanical observable for atom charges in a molecular system, there is no original definition for quantum charges. Charges on atoms are assigned using population analysis methods. The partial atomic charge of an electron density covered positively charged atomic center Z_A is defined as [50]

$$(q)_A = Z_A - \int \rho_A(r) dr, \quad (2.23)$$

where $(q)_A$ denotes the atomic charge and Z_A denotes the charge on the nucleus of an atom A. The total number of electrons in the system (N) is the second term in Equation (2.23) and can be expressed as

$$N = \sum_{\mu}^{AO} (PS)_{\mu\mu}, \quad (2.24)$$

P denotes the electron density and S is the overlap population.

The new Charge Model 5 (CM5) model generates class IV partial atomic charges by mapping from Hirshfeld population analysis of density functional electronic charge distributions. The CM5 model is applicable to any charged or uncharged molecule made of any periodic table element in the gas phase or solution.

The CM5 model predicts dipole moments for the tested molecules that are more accurate than those predicted by the original Hirshfeld approach or many other common methods such as atomic polar tensor and Löwdin, Mulliken, and natural population studies. Furthermore, the CM5 charge model is mostly independent of a basis set. It may be utilized with bigger basis sets; hence this model outperforms the earlier charge models CMx (x = 1-4 or 4M) and other methods that are susceptible to basis set sensitivities. Atomic charges in a molecule (neutral or ionic) are defined by the following equations in the CM5 model:

$$q_k^{CM5} = q_k^{HPA} + \sum_{k' \neq k} T_{kk'} B_{kk'} , \quad (2.25)$$

$$B_{kk'} = \exp [-\alpha(r_{kk'} - R_{Z_k} - R_{Z_{k'}})] , \quad (2.26)$$

where k and k' are indexes that cover all atoms in the molecule. R_Z is the atomic covalent radius, and Z_k and $Z_{k'}$ are the corresponding atomic numbers. q_k^{HPA} is the partial atomic charge from population analysis by Hirshfeld (HPA). The values where $T_{kk'} = -T_{k'k}$ are model parameters that must be determined. The quantity $B_{kk'}$ refers the Pauling bond order [51]. The CM5 model uses the Pauling bond order, which is based only on molecular geometry, rather than electronic-structure bond orders, such as the Mayer bond [52-54] order utilized in previous CMx models. This modification substantially simplifies the mapping of class II charges without compromising accuracy, making a CM5 calculation less computationally intensive. It should result in a faster and more stable convergence of a self-consistent reaction field process inside the extended Born dielectric continuum approximation, where the reaction field depends on the atomic charges [55].

3. LITERATURE BACKGROUND

3.1. Catalysis

Catalysis is a crucial area of chemistry [56-58]. Berzelius proposed the word "catalysis" in 1836, derived from the Greek word "καταλεινν" (=loose down, dissolve), to explain well-known experimental findings such as wine and beer fermentation and sulfuric acid (oil of vitriol) synthesis, starch transformation to sugar by acids, H₂O₂ decomposition by metals, ethanol oxidation to acetic acid on Pt, and so on. Catalysis, by definition, is a process in which the rate of a reaction is increased by a little amount of the so-called catalyst, which theoretically does not vary during the reaction, in contrast to surface or stoichiometric reactions. Some 60 years later, Berzelius recognized the kinetic nature of this process and defined it in 1895: "*a catalyst is a substance that modifies the rate of a chemical reaction without appearing in the products.*" A catalyst, according to IUPAC (1976), is a substance that, when present in small amounts, speeds up the process of reaching chemical equilibrium without incurring chemical change [59]. It has been established that the catalyst works by lowering the energy required to progress along the reaction pathway, i.e., the activation energy E_a that must be overcome to yield products. This activation energy is the amount of energy necessary to break through the reaction barrier and influences how quickly a reaction proceeds. In other words, the reaction will be faster, if the activation barrier is lower. It is important to note that the thermodynamics of the reaction are unaffected by catalyst action, and the resultant effect is that the catalyst influences only the reaction rate.

Catalysis can be divided into two forms based on the relationships between the phases of catalysts and reactants, namely homogeneous and heterogeneous catalysis [60]. In homogeneous catalysis, catalysts are in the same phase as the reactants, and often the products as well, allowing for enough contact between the catalyst and the reactant, resulting in high catalytic efficiency. Many homogeneous catalysts are made up of a (transition) metal atom or a cluster of a few atoms that are stabilized by suitable ligands. As a result, active sites can be used effectively and are easily identified. Furthermore, by modifying the ligand, the catalyst characteristics and catalytic performance can be rationally controlled.

As a result, homogeneous catalysts typically not only have the high activity but also extremely high, and most often adjustable, selectivity but the major issue of separating homogeneous catalysts from the raw materials and the products has limited their industrial application [61]. Heterogeneous catalysis, on the other hand, refers to all conditions in which catalysts and reactants are in different phases. Although heterogeneous catalysts are typically less active and/or selective than homogeneous catalysts, they are more stable and easier to remove from the reaction system. As a result, most industrial catalysis is currently based on heterogeneous catalysis methods [62]. To make use of the benefits of both homogeneous and heterogeneous catalysts, heterogenization of homogeneous catalysts has been explored since the late 1960s, often by attaching the homogeneous catalyst to an insoluble substrate via various physical or chemical interactions, a process known as homogeneous catalyst heterogenization [63]. This process is quite appealing and has been thoroughly investigated. However, decades of research have shown that it is incredibly difficult for a variety of reasons [64]. Nonetheless, newly developed single atom catalysis may give an alternative to heterogenization of homogeneous catalysts and may serve as a bridge between homogeneous and heterogeneous catalysis.

3.1.1. Single Atom Catalysis

The term “single-atom catalysis” was first introduced in 2011 by Prof Zhang Tao and coworkers [65]. Single atom catalysis refers to catalysis using a "single atom catalyst" (SAC), which is a catalyst made up of exclusively isolated single atoms spread on a substrate [66]. This concept has sparked a lot of interest in the field because SACs considerably improve the utilization rate of the catalysts' active components. The most important characteristic of SACs is that they have isolated, individual atoms dispersed on the support, which not only maximizes the metal's atomic efficiency but also gives more uniform, well-defined active sites than common heterogeneous catalysts, which have a variety of active sites [67]. For many reactions, this makes SACs more active and selective than typical heterogeneous nanocatalysts, and they act like homogeneous catalysts in terms of both local structure and catalytic activity.

In summary, SACs are heterogeneous catalysts and hence highly stable and easy to separate; at the same time, they have isolated active sites comparable to homogeneous catalysts, giving them the advantages of both homogeneous and heterogeneous catalysts.

SACs with atomically distributed metals have been developed as a brand-new class of heterogeneous catalysts, attracting great deal of interest owing to their enhanced atomic usage catalytically active metals. The first atomically distributed heterogeneous catalysts were developed in the 1990s [68]. With the passing of time, new advancements in the study of SACs have been made. Yan *et al.* [69] employed graphene as the carrier and took advantage of its unique features to create a Pd₁/graphene SAC for the selective hydrogenation of 1,3-butadiene in 2015.

Over the last three decades, computational chemistry has evolved into a strong tool for investigating the fundamental stages and mechanisms of many catalytic reactions at the atomic scale, which are difficult to research experimentally [70-72]. The use of theoretical calculations, particularly density functional theory (DFT) modelling, to identify the nature of active sites and reaction processes in the context of SACs is particularly beneficial.

3.1.2. The Application of SACs in Selective Hydrogenation

SACs have been demonstrated to have higher catalytic performance in a variety of processes, including ammonia synthesis [73-74], selective hydrogenation [75-77], CO oxidation [78-79], CO₂ conversion [80-81] and (reverse) water-gas shift reactions [82-84]. Selective hydrogenation is frequently utilized in medicine, chemical manufacturing, printing and dyeing, health-care products, and other industries. There are various types of selective hydrogenation, as demonstrated in Figure 3.1, including alkyne (C≡C), alkadiene (C=C), nitrogen–oxygen unsaturated bond (N=O), carbon–oxygen unsaturated bond (C=O), and carbon–nitrogen unsaturated bond (C=N) hydrogenations [85]. The term "selective hydrogenation" refers to the hydrogenation of only one of the functional groups when there are two or more unsaturated functional groups in substrates, or when the catalytic system contains distinct unsaturated substrates [86].

When both alkynes and alkenes are present, selective hydrogenation can only be implemented on the alkynes. Thus, in most chemical synthesis processes, selective hydrogenation is the best option. In industrial production, the Pd/CaCO₃ (Lindlar catalyst) catalyst is the most extensively employed [87-89].

The supported metal cluster catalyst's high activity is attributable to the presence of well distributed nanoclusters in the form of metal active components on the carrier with a high specific surface area, which can effectively use the catalytically active sites and enhance the catalyst's reaction activity [90-91].

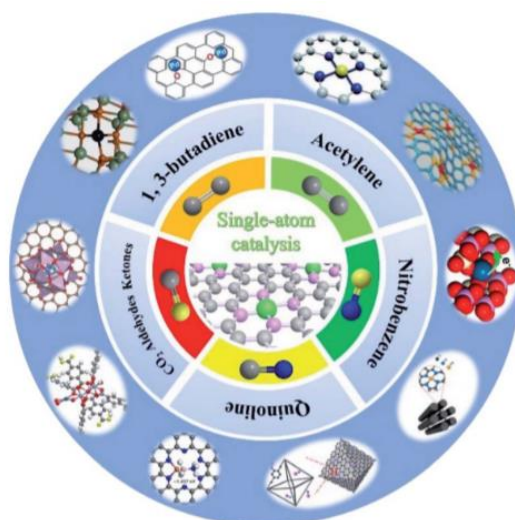


Figure 3.1. Diagram of single atom catalysts for various types of selective hydrogenation [85].

However, using precious metal resources to provide catalyst selectivity at the cost of activity is wasteful [92]. For instance, Palladium (Pd) is a pricey heavy metal that is also extremely detrimental to the environment [93-94]. Furthermore, despite their small size, nanocatalysts have several active centers and are not the most efficient active sites. As a result, researchers have been progressively lower the size of active metal particles to generate SACs with 100% atom utilization, driven by the maximal development and use of metal atoms [95].

3.1.2.1. Selective Hydrogenation of Alkynes. Semihydrogenation of acetylene is a common industrial method for removing trace acetylene from crude ethylene. Pd-based catalysts have been shown to be effective for acetylene conversion, however increasing selectivity to ethylene is difficult [96]. Li and colleagues [97] revealed that PdIn(110) with single-atom Pd sites is more selective towards ethylene than Pd₃In(111) with adjacent Pd trimer sites relying on DFT modeling, which is supported by experimental data. In PdIn(110), C₂H₂ adsorbs on two neighboring Pd atoms, whereas C₂H₄ coordinates on one Pd atom via weak π bonding. The adsorption energy of intermediates and the hydrogenation barrier of elementary stages indicate that semihydrogenation of acetylene and desorption of ethylene are both simple processes (Figure 3.2) [97]

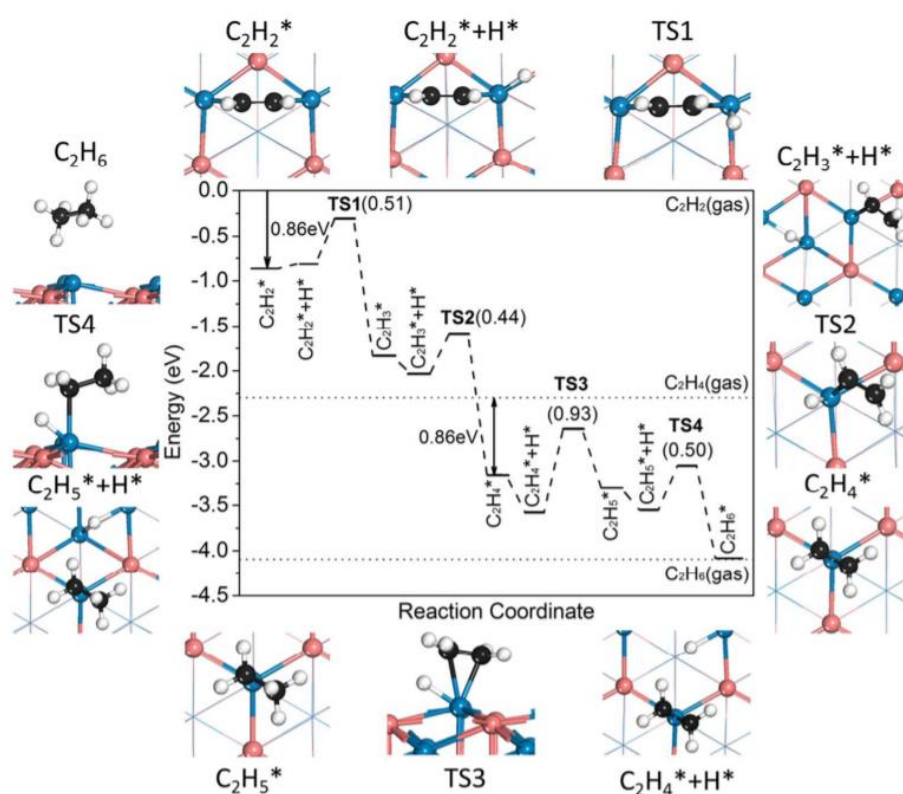


Figure 3.2. Hydrogenation mechanism of acetylene to ethane on the PdIn(110) surface [97].

4. RESULTS

4.1. Computational Procedure

Density functional theory (DFT) techniques have been used since they are computationally cost effective for the integration of electron correlation effects to complex systems [98].

In this study, the PBE [99] exchange correlation functional was used. The 6-31G(d,p) basis set for H, C, O, Al, Si as well as LANL2DZ basis set of Hay and Wadt were used for Rh and Ir [100]. Metal clusters including transition metals are challenging systems for theoretical studies because they have partially filled *d shells* typically resulting in very narrow energy range [101,102]. Therefore, it is very important to determine appropriate methods for DFT calculations involving transition metals. In theoretical chemistry, the M06-2X and PBE functionals have been applied to predict structures and their energies [103,104]. The PBE functional has been widely used in the study of complexes and compounds containing transition metals [105]. Wang has reported the accuracy of the PBE functional for transition metals by performing computations on small scandium clusters. (Sc_n , $n=1-3$) [106]. Therefore, it's critical to figure out the best DFT methods for transition metal calculations [107]. The Gaussian 09 series of programs [108] were used to perform all calculations. The PBE functional, along with the standard 6-31G(d,p) basis set, were used to perform full geometrical optimizations and conformational searches for the transition state structures in vacuum [109]. All ground state geometries have been characterized with positive frequencies whereas transition states have one imaginary frequency. Charge analysis was carried out using charge model 5 (CM5). The ideal gas approximation at $T = 298.15$ K and 1 atm for vacuum calculations was used.

4.2. Usage of zeolite supported-Rh(C₂H₂)₂ as a catalyst

In this study, the structure-catalytic property connections for zeolite supported rhodium and iridium complexes are utilized to catalyze acetylene reactions. Because of its crystalline structure, *zeolite* was chosen as the support because it enables the production of structurally uniform supported species [110].

A simpler structure for computational efficiency is chosen. Besides from the zeolite support, the ligands include acetylene (C₂H₂) modulates reactivity through electronic effects. The initial complex is shown in Figure 4.1 (the one on the right is Rh(C₂H₂)₂ on simpler zeolite structure and the one on the left is Rh(C₂H₂)₂ on crystal structure of silicalite faujasite).

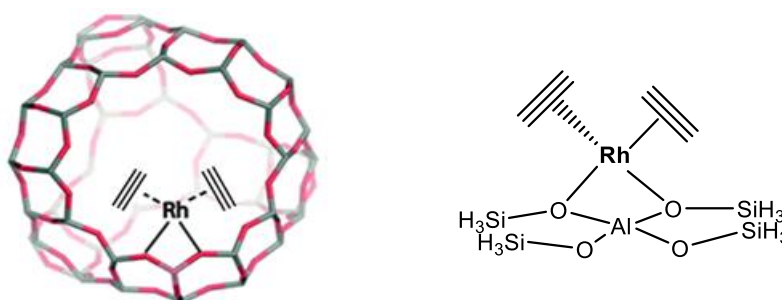


Figure 4.1. 3D structure (left) and 2D model (right) of the Rh(C₂H₂)₂-zeolite complex.

First of all, the reaction mechanism of the hydrogenation of acetylene on the zeolite supported Rh complexes was modeled in Figure 4.2. According to the mechanism, in complex 1, coordination of H₂ to the Rh center in trans position to the acetylene leads to formation of complex 2. Complex 2 is transformed to species 3 by an oxidative addition of H₂ to the Rh center. From 3 to complex 4, insertion of alkyne to the metal H bond is observed; then, one of the hydrogens is captured by one acetylene group to give one ethylene group which is complex 5.

3D ground state geometries of (1-3), (4-6) and (7-9) with CM5 charges on Rh metal are shown in Table 4.1, Table 4.2, and Table 4.3 respectively. It is observed that complex 4 has the highest positive charge and complex 9 has the lowest positive charge in Table 4.2 and Table 4.3.

Transition state geometries of Path 1 are also given in Table 4.4. From complex 5, the insertion of H_2 leads to formation of complex 6. In this case, one of the hydrogens is captured by ethylene group to form complex 9 which has one acetylene and one ethane group.

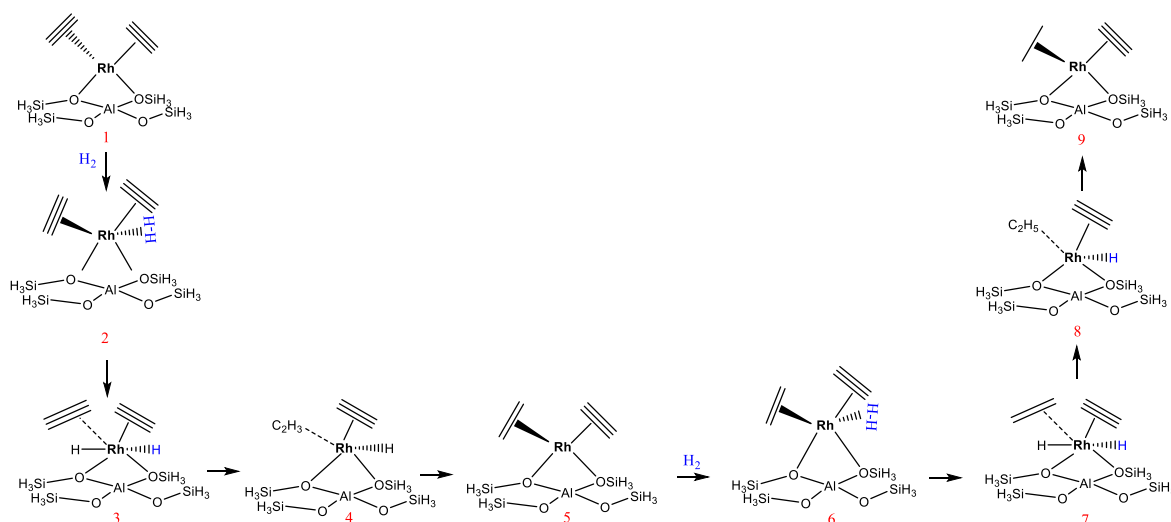


Figure 4.2. 2D mechanism for the hydrogenation of acetylene on the zeolite supported Rh complexes (Path 1).

During C_2H_2 hydrogenation reactions ($C_2H_2 + H_2 \rightarrow C_2H_4$) on Rh metal surface, C_2H_2 and H_2 molecules are firstly co-adsorbed on the same site. After the dissociation of H_2 molecule as two H atoms, one of them combines with C_2H_2 to generate the intermediate product C_2H_3 . Then, C_2H_3 reacts with the other H atom to form the final product C_2H_4 . The reaction process of C_2H_4 hydrogenation ($C_2H_4 + H_2 \rightarrow C_2H_6$) is analogous to that of C_2H_2 hydrogenation. C_2H_5 and C_2H_6 molecules serve as intermediate and end products in these saturation hydrogenation processes, respectively. After the complex 8 is formed, although H is closer to C_2H_2 with 2.09 Å, it is captured by C_2H_5 group with 2.39 Å rather than C_2H_2 .

Table 4.1. Ground state geometries, bond distances (Å) and CM5 charges of (1-3).

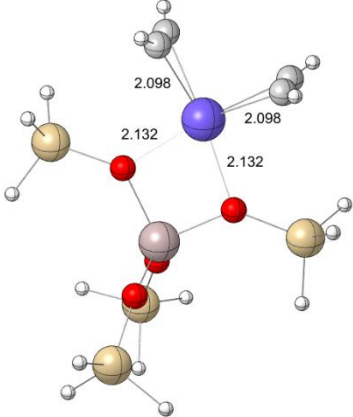
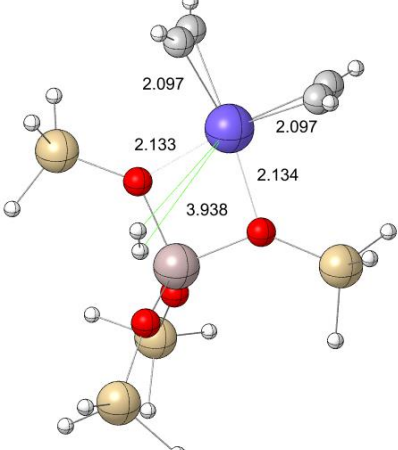
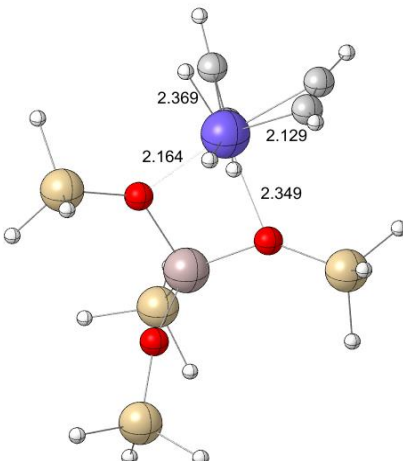
Molecule ID	3D Ground State Molecules	CM5 Charge on Rh metal
1		0.5336
2		0.5329
3		0.4375

Table 4.2. Ground state geometries, bond distances (Å) and CM5 charges of (4-6).

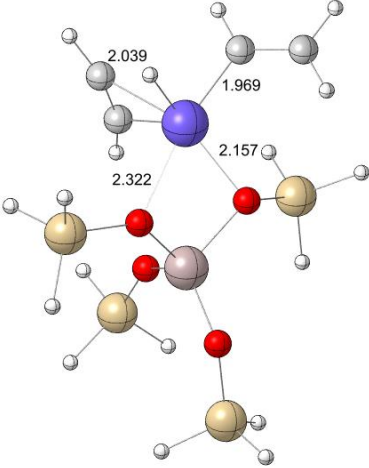
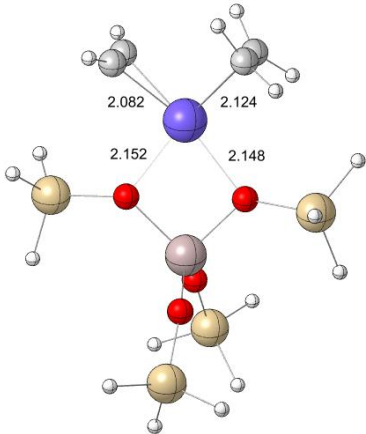
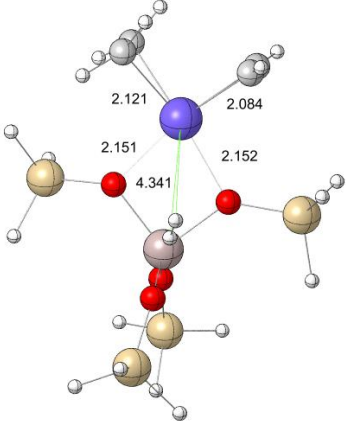
Molecule ID	3D Ground State Geometries	CM5 Charge on Rh metal
4	 <p>3D ball-and-stick model of molecule 4. The central Rhodium (Rh) atom is shown in blue. It is coordinated to two nitrogen atoms (grey) and two oxygen atoms (red). The bond distances are labeled as 2.039 Å, 1.969 Å, 2.157 Å, and 2.322 Å. The molecule also contains two methyl groups (yellow and white).</p>	0.5608
5	 <p>3D ball-and-stick model of molecule 5. The central Rhodium (Rh) atom is shown in blue. It is coordinated to two nitrogen atoms (grey) and two oxygen atoms (red). The bond distances are labeled as 2.082 Å, 2.124 Å, 2.152 Å, and 2.148 Å. The molecule also contains two methyl groups (yellow and white).</p>	0.5361
6	 <p>3D ball-and-stick model of molecule 6. The central Rhodium (Rh) atom is shown in blue. It is coordinated to two nitrogen atoms (grey) and two oxygen atoms (red). The bond distances are labeled as 2.121 Å, 2.084 Å, 2.151 Å, 2.152 Å, and 4.341 Å. The molecule also contains two methyl groups (yellow and white).</p>	0.5352

Table 4.3. Ground state geometries, bond distances (Å) and CM5 charges of (7-9).

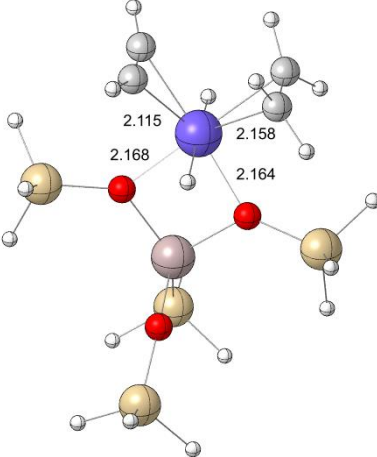
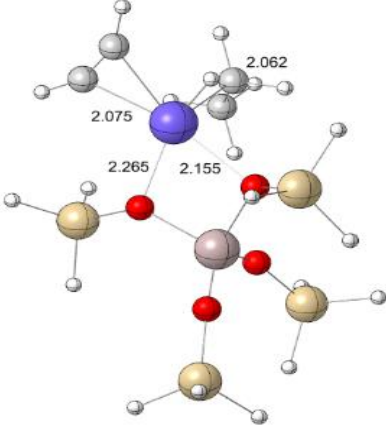
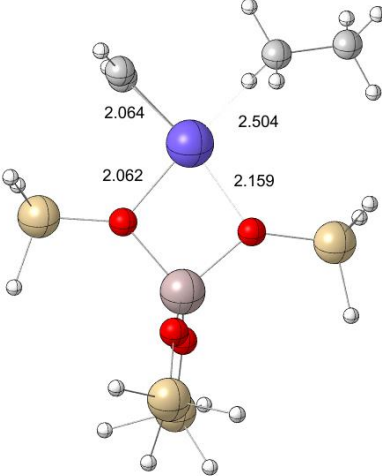
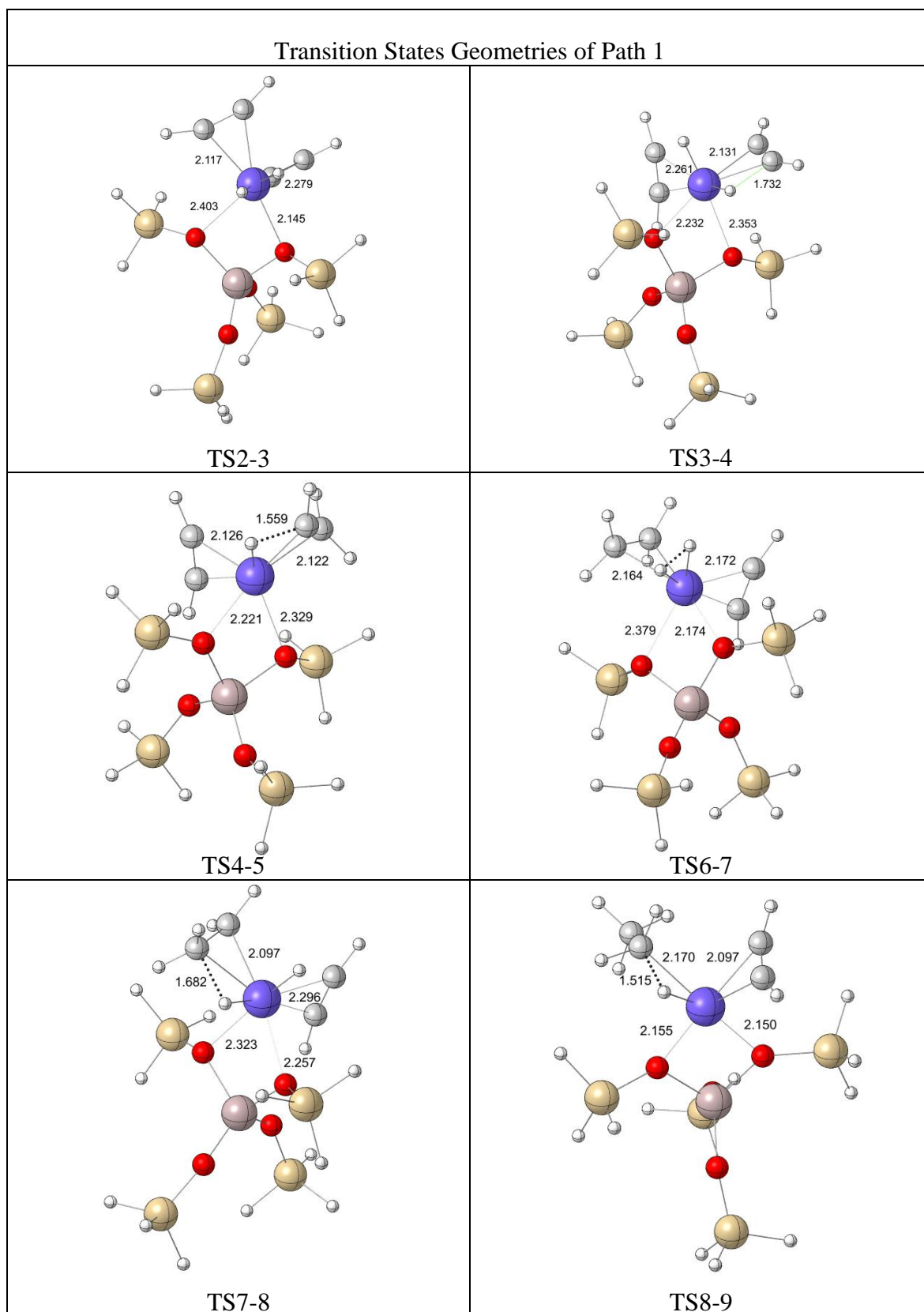
Molecule ID	3D Ground State Geometries	CM5 Charge on Rh metal
7	 <p>3D ball-and-stick model of molecule 7. The central Rhodium (Rh) atom is shown in blue. Bond distances are labeled: 2.115 Å (Rh-N), 2.158 Å (Rh-N), 2.168 Å (Rh-O), and 2.164 Å (Rh-O).</p>	0.5255
8	 <p>3D ball-and-stick model of molecule 8. The central Rhodium (Rh) atom is shown in blue. Bond distances are labeled: 2.075 Å (Rh-N), 2.062 Å (Rh-N), 2.265 Å (Rh-O), and 2.155 Å (Rh-O).</p>	0.5020
9	 <p>3D ball-and-stick model of molecule 9. The central Rhodium (Rh) atom is shown in blue. Bond distances are labeled: 2.064 Å (Rh-N), 2.504 Å (Rh-N), 2.062 Å (Rh-O), and 2.159 Å (Rh-O).</p>	0.4369

Table 4.4. Transition state geometries and bond distances (Å) for Path 1.



From these calculations and optimizations, the potential energy surface (PES) diagram is shown in Figure 4.3 by examining the relative Gibbs free energies of both ground and transition states from complex 1 to complex 9 (Path 1).

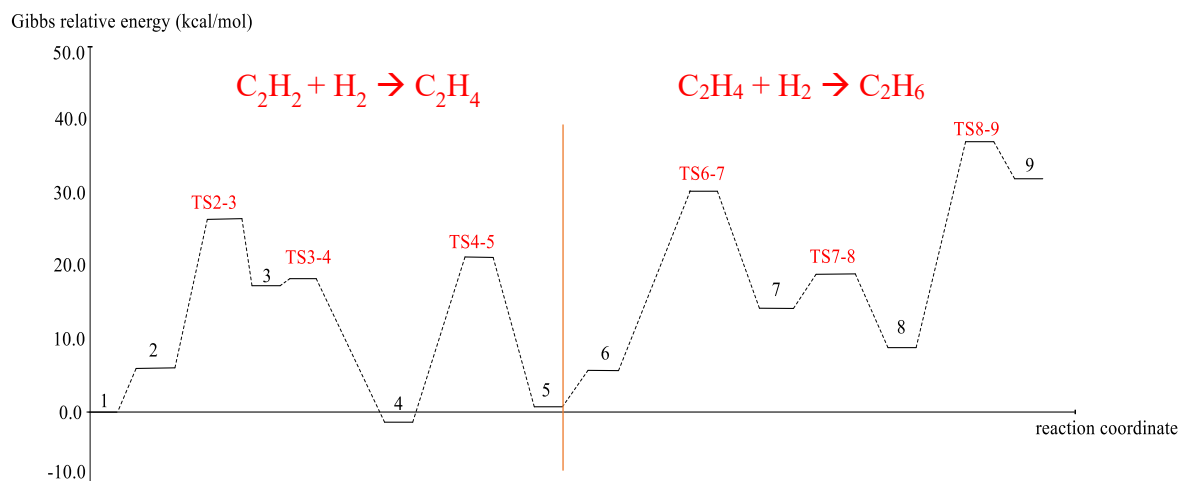


Figure 4.3. Potential energy surface diagram for the acetylene hydrogenation of zeolite-supported complexes (Path 1).

According to the PES diagram from Figure 4.3, when sufficient hydrogen is given, the produced ethylene can be further hydrogenated to ethane because it is still an unsaturated hydrocarbon. However, ethylene can take priority over hydrogenation in terms of desorption from surfaces if its hydrogenation barrier is larger than its desorption barrier [111]. Thus, the hydrogenation process of ethylene was also calculated. A surface vinyl (C_2H_3) intermediate ($3 \rightarrow TS3-4$) is formed when a hydrogen atom on the metal reacts with acetylene. The distance between the nearest hydrogen atom and the acetylene is examined to find the intermediate structure, and an initial estimate for the intermediate structure is determined. Therefore, the surface vinyl intermediate is optimized on the complex to determine its most stable structure and its relative energy is calculated as 18.5 kcal/mol. In addition, from the diagram, it is easy to observe that the partial hydrogenation of one C_2H_2 (acetylene) to C_2H_4 (ethylene) ($1 \rightarrow 5$) is facile since the $4 \rightarrow TS4-5$ barrier is 20.9 kcal/mol. However, the rate determining step is $8 \rightarrow TS8-9$ step since it has the highest activation energy barrier (28.7 kcal/mol) among all steps.

The ethyl on the surface tilts along the Rh metal, bringing it closer to one side. This indicates that the Rh atom interacts more strongly with the surface ethyl. Surface ethyl has Rh-C length of 2.062 Å which is the shortest Rh-C bond in the mechanism. The Rh-C bond aids in stabilizing the CH₂ group's electron deficiency in the ethyl intermediate. The reduced contact between H atoms and C₂H₄ raises the hydrogenation barriers, making over-hydrogenation of C₂H₄ difficult. The activation energy of this barrier is calculated as 28.7 kcal/mol where the highest point of the profile is the TS8-9 for the insertion of an alkyne to the metal Rh center. Ethane is produced when a surface ethyl intermediate reacts with atomic hydrogen. The result shows that ethane adsorption on Rh metal is not stable due to the steric hinderance. The activation energy for ethane production (second stage) is higher than that for acetylene to ethylene hydrogenation. Therefore, it is difficult for the reaction to generate complex 9 from complex 5. As a result, in line with the purpose of the study, ethylene production is selective rather than ethane production for Path 1. In other words, hydrogenation of ethylene to ethane is not observed easily because of high activation energy barrier. Uzun *et al.* have studied experimentally zeolite supported Rh catalyst and their finding is such that the ethylene selectivity is 88.1%. In addition, the regeneration of the catalyst and the emission of C₂H₄ (ethylene) via reaction mechanism (Path 1A) is analyzed. The reaction pathway from complex 5 to complex 1 is shown in Figure 4.4. The replacement of ethylene on Rh metal with the acetylene group in the reactor is investigated.

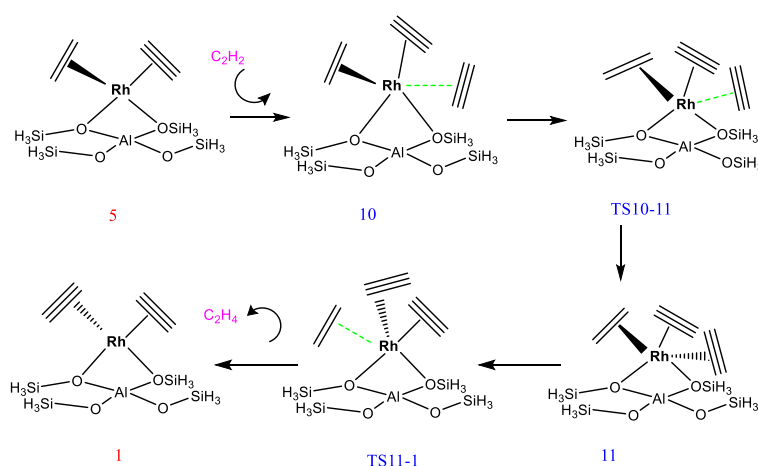
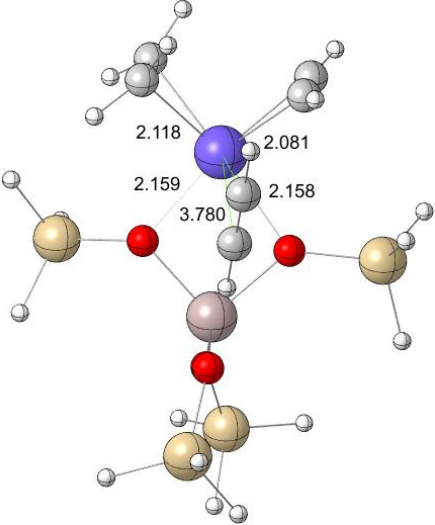
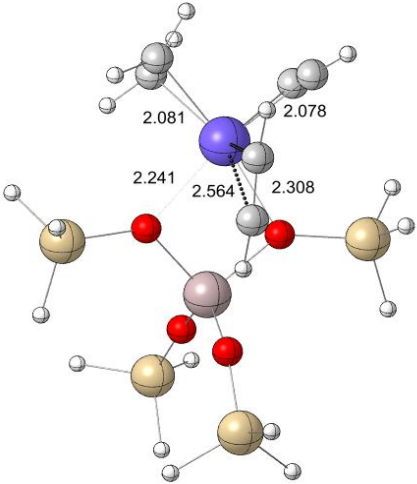
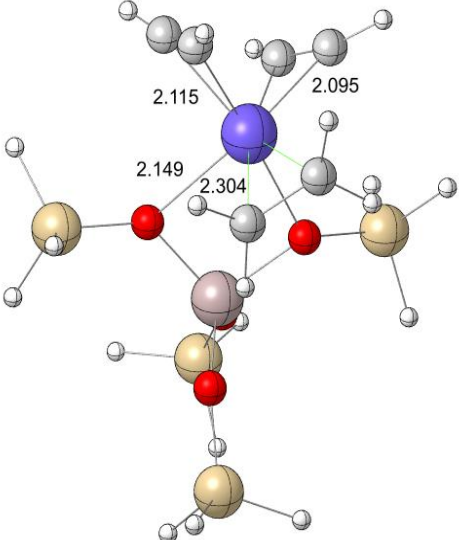
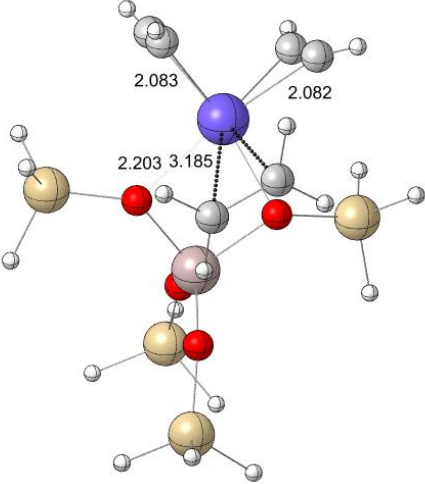


Figure 4.4. 2D mechanism for the replacement of ethylene with acetylene on the zeolite supported Rh complexes (Path 1A).

Figure 4.4 explains that the presence of C_2H_2 (acetylene) group can relocate with the currently found C_2H_4 (ethylene) group on the Rh metal. The ground and transition state geometries of Path 1A are given in Table 4.5.

Table 4.5. Ground and transition state geometries and bond distances (\AA) for Path 1A.

Ground State Geometries	Transition State Geometries
 <p style="text-align: center;">10</p>	 <p style="text-align: center;">TS10-11</p>
 <p style="text-align: center;">11</p>	 <p style="text-align: center;">TS11-1</p>

The PES diagram of Path 1A supports the pathway (Figure 4.5). According to this path, C_2H_4 (ethylene) is released easily since it has relatively low (8.7 kcal/mol) activation energy barrier from 10→TS10-11. Moreover, the catalyst which is complex 1 is regenerated at the end.

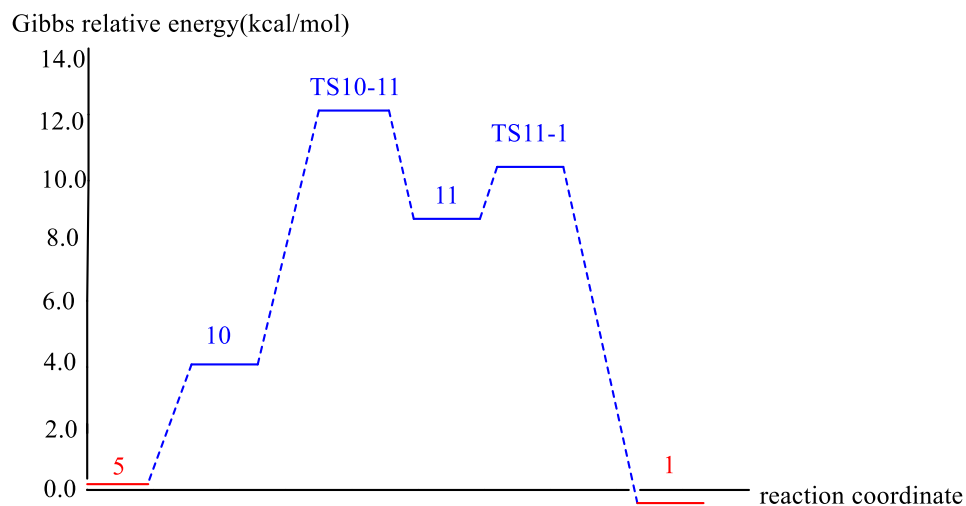


Figure 4.5. Potential energy surface diagram for the regeneration of the catalyst and emission of ethylene (Path 1A).

The reaction pathway from complex 5 to complex 1 which is Path 1A and the reaction pathway which is Path 1 are demonstrated together in Figure 4.6. In the reaction medium, there are enough H_2 and C_2H_2 , so after the complex 5 is produced there are two competitive pathways; either Path 1 or Path 1A is traced.

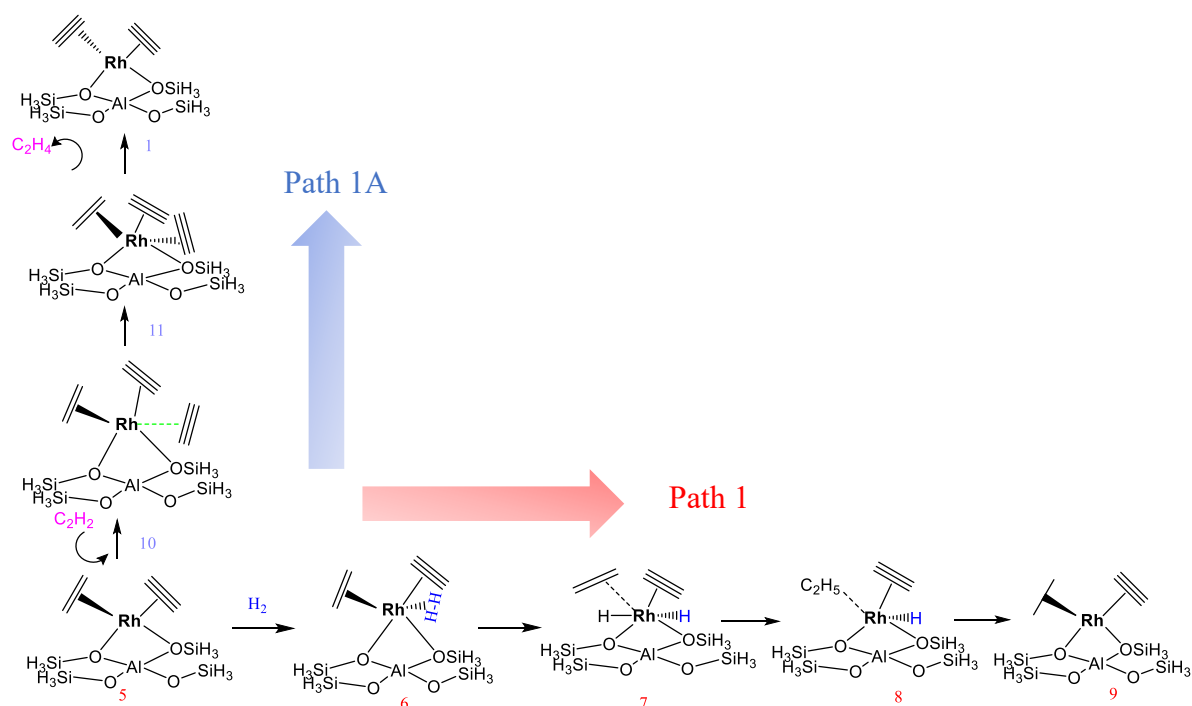


Figure 4.6. Comparison of the 2-D mechanisms of Path 1 for the hydrogenation of acetylene and Path 1A for the regeneration of the catalyst in the zeolite supported Rh complexes.

As the potential energy surface diagram (Figure 4.7) is plotted by calculating relative Gibbs free energy of ground and transition states, it is seen that Path 1A is energetically more favorable than Path 1 by comparing their relative energies. The activation energy barrier of TS10-11 (8.7 kcal/mol) is lower than the activation energy barrier of TS6-7 (28.7 kcal/mol). Therefore, reaction pathway prefers proceeding Path 1A. As a result, catalyst is regenerated and C_2H_4 is emitted from the reactor.

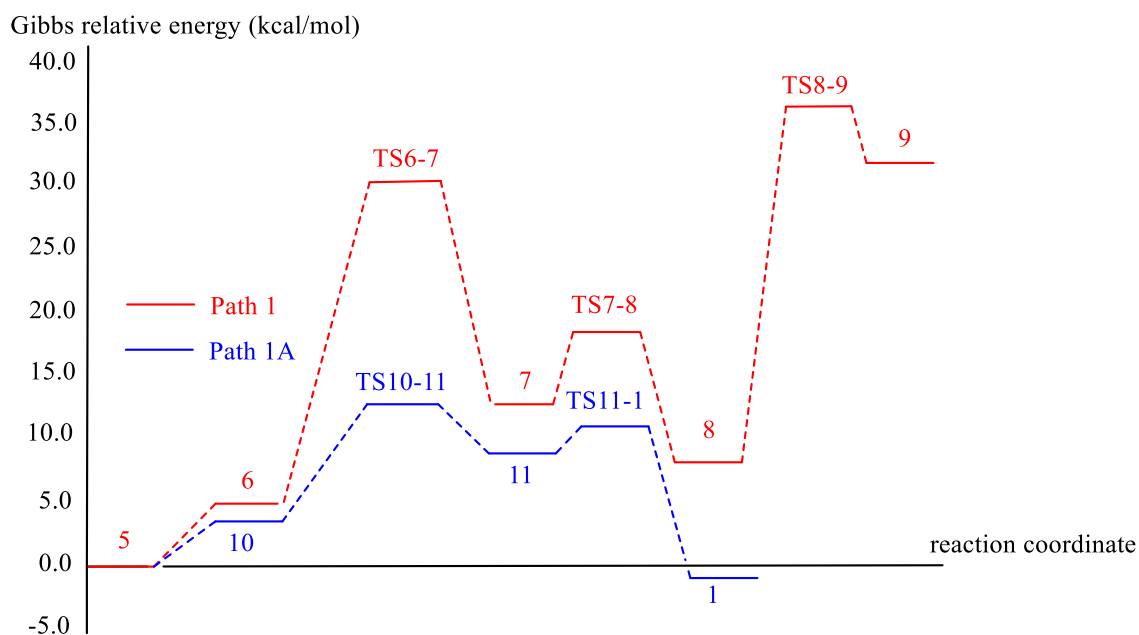


Figure 4.7. Potential energy surface diagram of Path 1 and Path 1A.

In addition, the regeneration of the catalyst and the emission of C_2H_6 (ethane) via reaction mechanism is analyzed as well. The reaction pathway from complex 9 to complex 1 (Path 1B) is shown in Figure 4.8. The replacement of ethane on Rh metal with the acetylene group in the reactor is investigated. The ground and transition state geometries of Path 1B are given in Table 4.6.

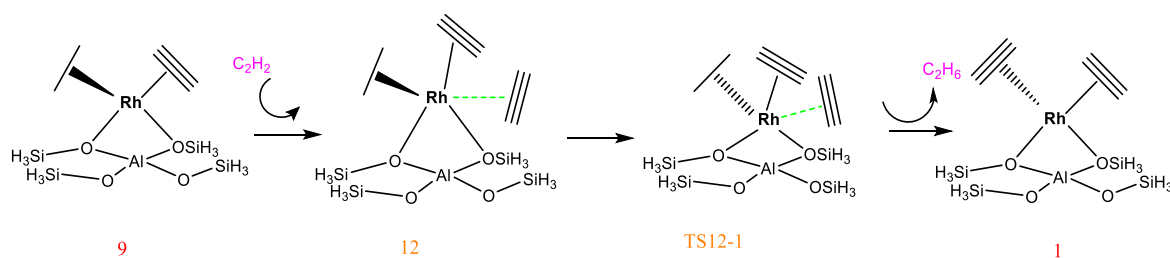
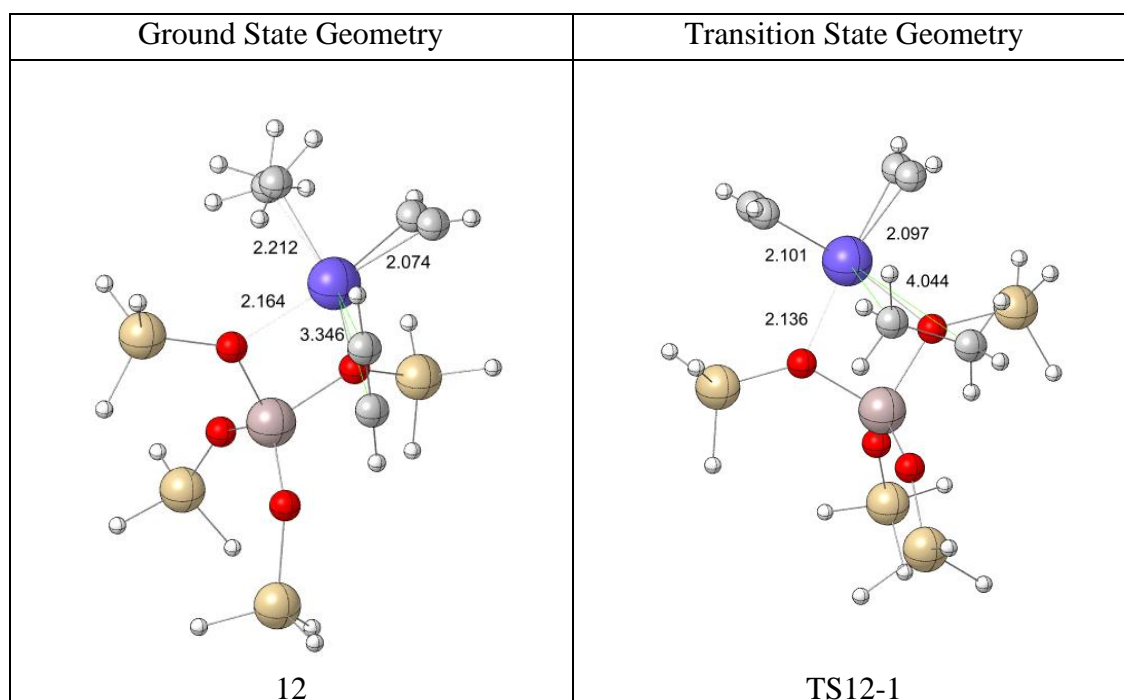


Figure 4.8. 2D mechanism for the replacement of acetylene with ethane on the zeolite supported Rh complexes (Path 1B).

Table 4.6. Ground and transition state geometries and bond distances (Å) for Path 1B.



According to the PES diagram (Figure 4.9) of Path 1B, the activation energy barrier from 12→TS12-1 is 8.9 kcal/mol which is relatively low. If the ethane is released; in other words, complex 9 is formed, it is easy to regenerate the catalyst since the reaction is exergonic with -32.7 kcal/mol energy.

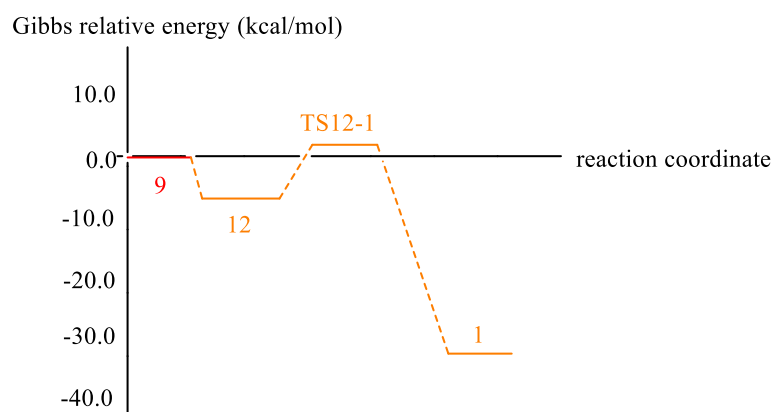


Figure 4.9. Potential energy surface diagram for the regeneration of the catalyst and emission of ethane (Path 1B).

From the hydrogenation mechanism of acetylene of Path 1, the coordination of second H_2 to complex 5, leads to formation of complex 6 and then complex 7 by oxidative addition. When the complex 7 is formed, hydrogen can be captured by ethylene group or acetylene group. If the H_2 is captured by ethylene group, Path 1 is followed. If the H_2 is captured by acetylene group, Path 2 is followed (Figure 4.10). Therefore, both Path 1 and Path 2 are modeled to figure out which path is more favorable. The potential energy surface (PES) diagrams are shown in Figure 4.11 by indicating the relative Gibbs free energies of both ground and transition states for Path 1 and Path 2. According to PES diagram, the energy barrier of Path 2 is relatively low compared to Path 1 that is the energy barrier of TS7-14 is 5.6 kcal/mol whereas the energy barrier of TS8-9 is 34.4 kcal/mol. Therefore, the ethylene production yielding complex 15 is selective, rather than complex 9 which has ethane group on Rh metal.

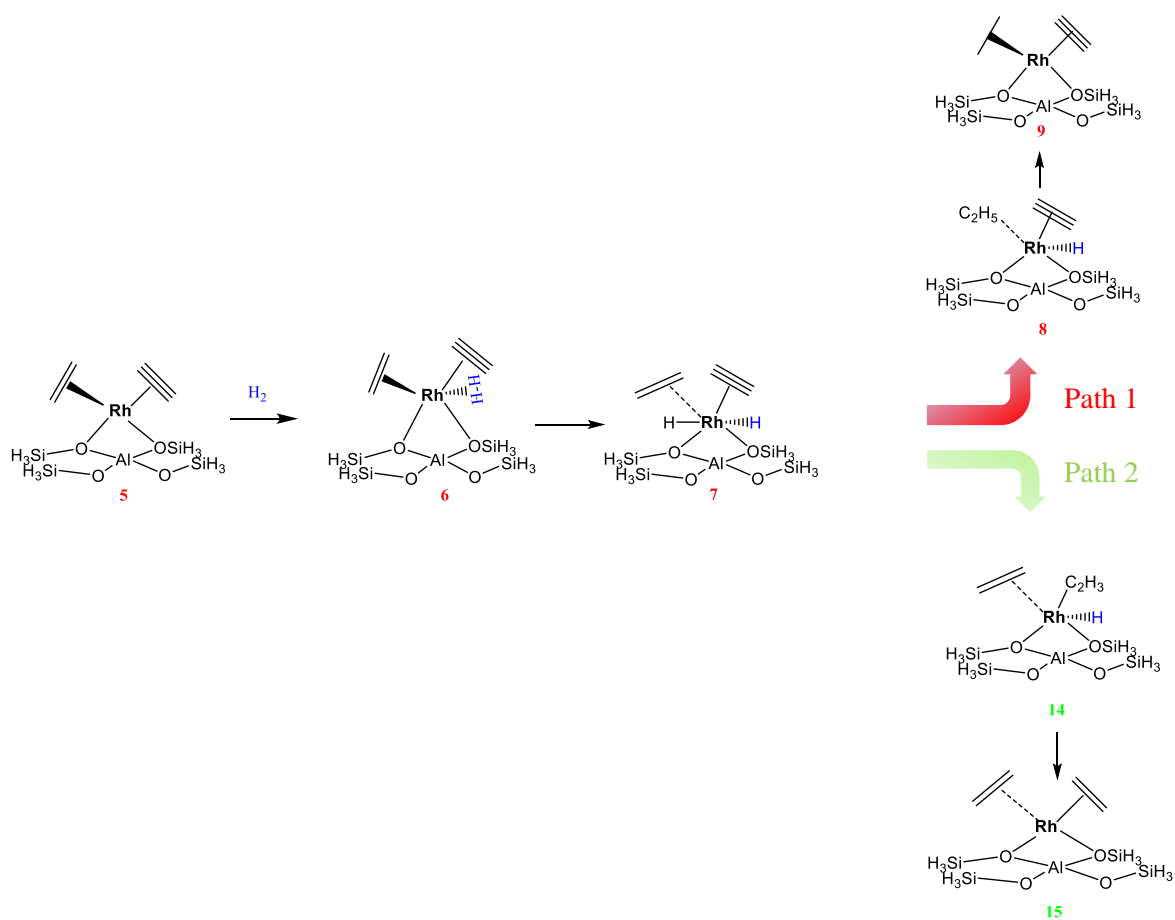
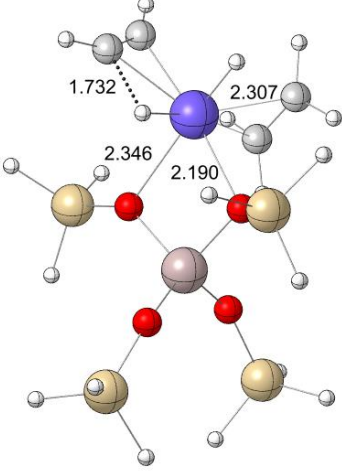
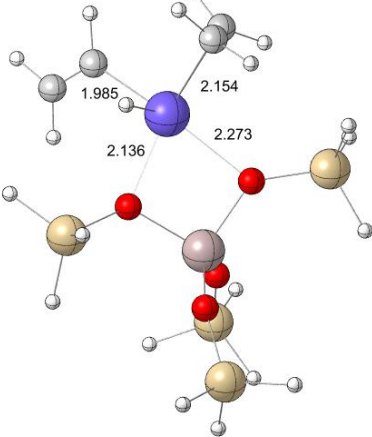
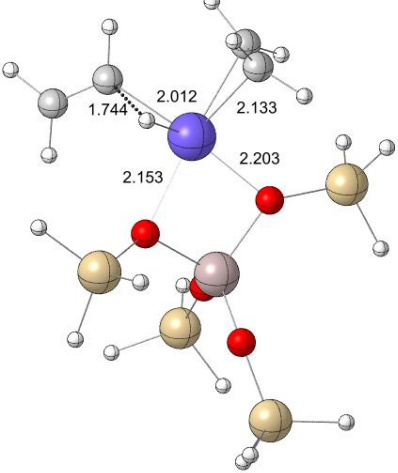
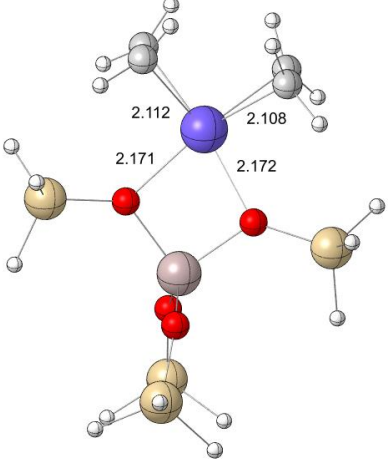


Figure 4.10. 2D mechanism of the hydrogenation of ethylene or acetylene on the zeolite supported Rh complexes.

Table 4.7. Ground and transition state geometries and bond distances (Å) for Path 2.

Transition State Geometries	Ground State Geometries
 <p>TS7-14</p> <p>Ball-and-stick model of the transition state TS7-14. The central blue atom is bonded to a grey atom (1.732 Å), a yellow atom (2.346 Å), and a red atom (2.190 Å). The red atom is also bonded to a grey atom (2.307 Å). Other atoms are shown in grey, yellow, and red.</p>	 <p>14</p> <p>Ball-and-stick model of the ground state 14. The central blue atom is bonded to a grey atom (1.985 Å) and a yellow atom (2.136 Å). The yellow atom is bonded to a red atom (2.273 Å). The red atom is also bonded to a grey atom (2.154 Å). Other atoms are shown in grey, yellow, and red.</p>
 <p>TS14-15</p> <p>Ball-and-stick model of the transition state TS14-15. The central blue atom is bonded to a grey atom (1.744 Å), a yellow atom (2.153 Å), and a red atom (2.203 Å). The red atom is also bonded to a grey atom (2.012 Å). Other atoms are shown in grey, yellow, and red.</p>	 <p>15</p> <p>Ball-and-stick model of the ground state 15. The central blue atom is bonded to a grey atom (2.112 Å) and a yellow atom (2.171 Å). The yellow atom is bonded to a red atom (2.172 Å). The red atom is also bonded to a grey atom (2.108 Å). Other atoms are shown in grey, yellow, and red.</p>

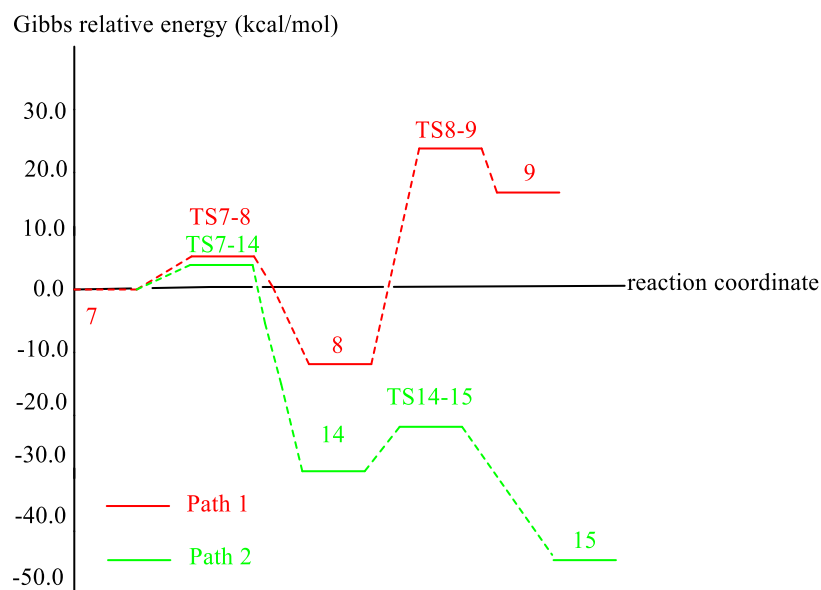


Figure 4.11. Potential energy surface diagram for the selectivity of acetylene versus ethylene for Path 1 and Path 2.

As complex 15 is produced, hydrogenation of ethylene groups (Path 2A) on the Rh metal is pursued in Figure 4.12.

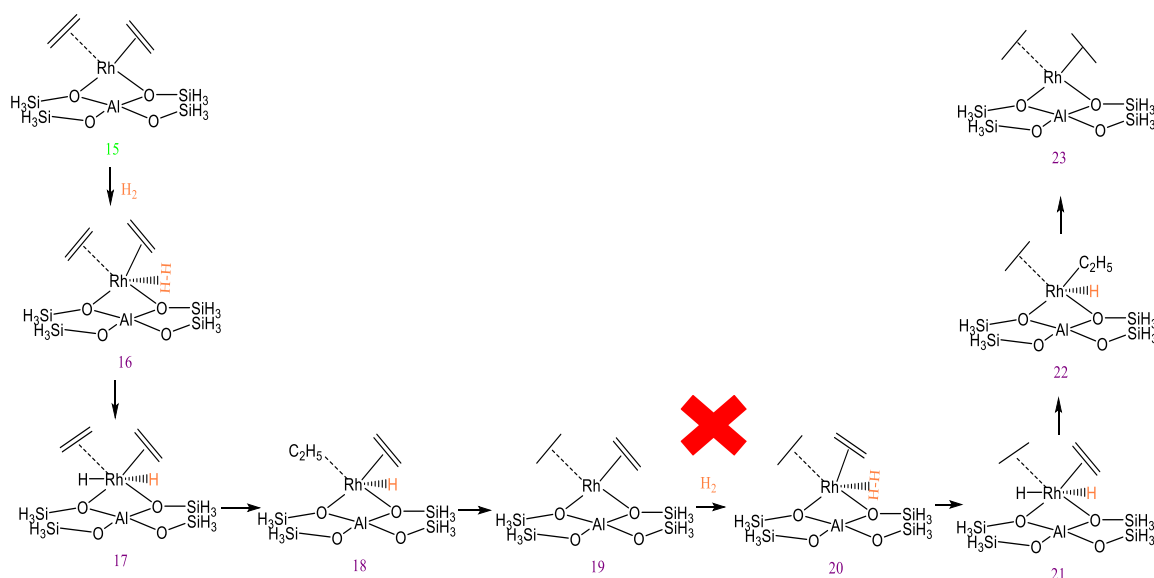


Figure 4.12. 2D mechanism for the hydrogenation of ethylene groups on the zeolite supported Rh complexes (Path 2A).

During C_2H_4 hydrogenation reactions ($C_2H_4 + H_2 \rightarrow C_2H_6$) on Rh metal surface, C_2H_4 and H_2 molecules are firstly co-adsorbed on the same site (16). After the dissociation of H_2 molecule as two H atoms (17), one of them combines with C_2H_4 to form the intermediate product C_2H_5 by oxidative addition (18). Then, C_2H_5 reacts with the other H atom to form the final product C_2H_6 . C_2H_5 and C_2H_6 molecules serve as intermediate and end products in these saturation hydrogenation processes, respectively. However, after 19 is generated, the pathway is unlikely to occur because the transition state, TS20-21, of ethane formation, is 27.8 kcal/mol from the potential energy surface diagram (Figure 4.13).

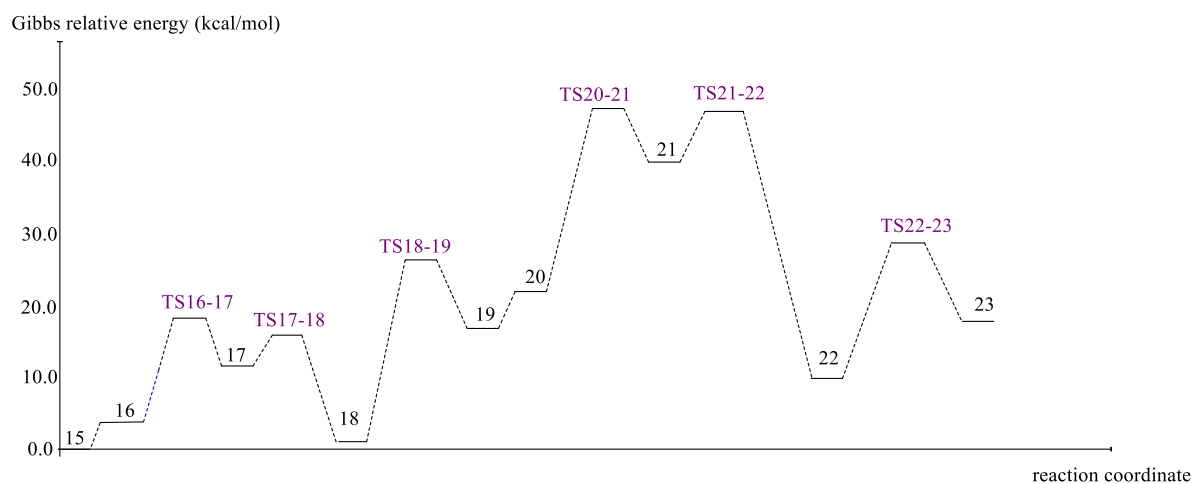


Figure 4.13. Potential energy surface diagram for the ethylene hydrogenation in zeolite-supported Rh complexes (Path 2A).

The coordination of a second H_2 molecule to the Rh center in complex 19 is slightly endergonic and yields complex 20. In any case, since ethane has no π bonds unlike acetylene and ethylene, it is difficult to be held on Rh metal; therefore, ethane is released as a gas and the formation of ethane from the intermediates is an endothermic process. 3D ground state geometries of (16-19) and transition state geometries of (TS16-17, TS17-18, TS18-19) are shown in Table 4.8 and Table 4.9 respectively.

Table 4.8. Ground state geometries and bond distances (Å) for Path 2A.

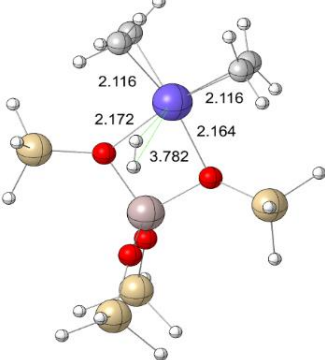
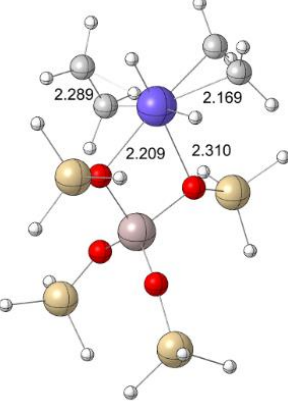
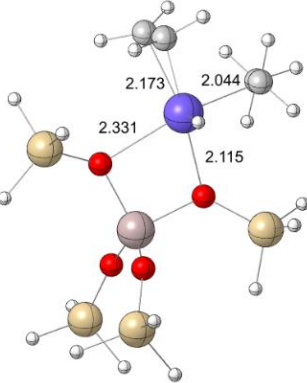
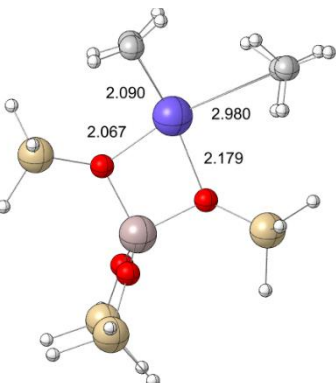
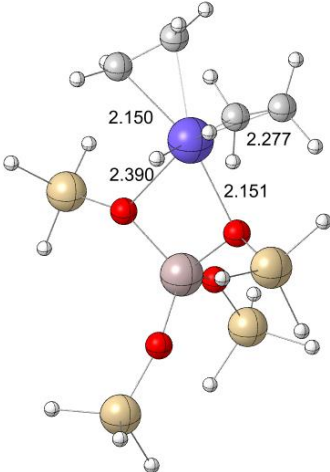
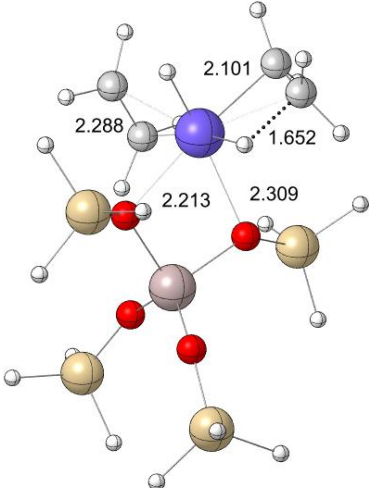
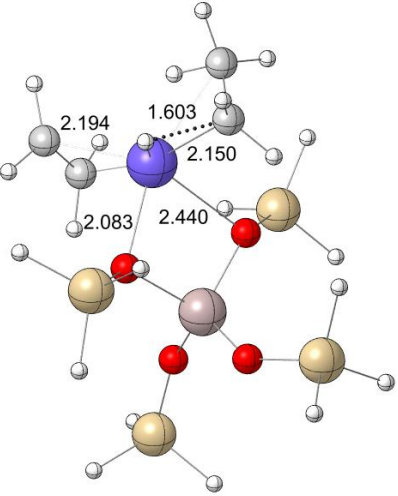
Molecule ID	Ground State Molecules
16	 <p>Ball-and-stick model of molecule 16. The central blue atom is bonded to two grey atoms (top) and two red atoms (middle). The bond distances are labeled as 2.116 Å (top-left), 2.172 Å (top-left to middle-left), 2.116 Å (top-right), and 2.164 Å (top-right to middle-right). A long bond of 3.782 Å connects the middle-left red atom to the middle-right red atom. The molecule also features two yellow atoms and several white hydrogen atoms.</p>
17	 <p>Ball-and-stick model of molecule 17. The central blue atom is bonded to two grey atoms (top) and two red atoms (middle). The bond distances are labeled as 2.289 Å (top-left), 2.169 Å (top-right), 2.209 Å (middle-left), and 2.310 Å (middle-right). The molecule also features two yellow atoms and several white hydrogen atoms.</p>
18	 <p>Ball-and-stick model of molecule 18. The central blue atom is bonded to two grey atoms (top) and two red atoms (middle). The bond distances are labeled as 2.173 Å (top-left), 2.044 Å (top-right), 2.331 Å (middle-left), and 2.115 Å (middle-right). The molecule also features two yellow atoms and several white hydrogen atoms.</p>
19	 <p>Ball-and-stick model of molecule 19. The central blue atom is bonded to two grey atoms (top) and two red atoms (middle). The bond distances are labeled as 2.090 Å (top-left), 2.980 Å (top-right), 2.067 Å (middle-left), and 2.179 Å (middle-right). The molecule also features two yellow atoms and several white hydrogen atoms.</p>

Table 4.9. Transition state geometries and bond distances (Å) for Path 2A.

Molecule ID	Ground State Molecules
TS16-17	
TS17-18	
TS18-19	

In addition, the regeneration of the catalyst and the emission of C_2H_6 (ethane) via reaction mechanism (Path 2B) is analyzed. The reaction pathway from complex 15 to complex 1 is shown in Figure 4.14. The replacement of two ethylene groups on Rh metal with the acetylene groups in the reactor is investigated.

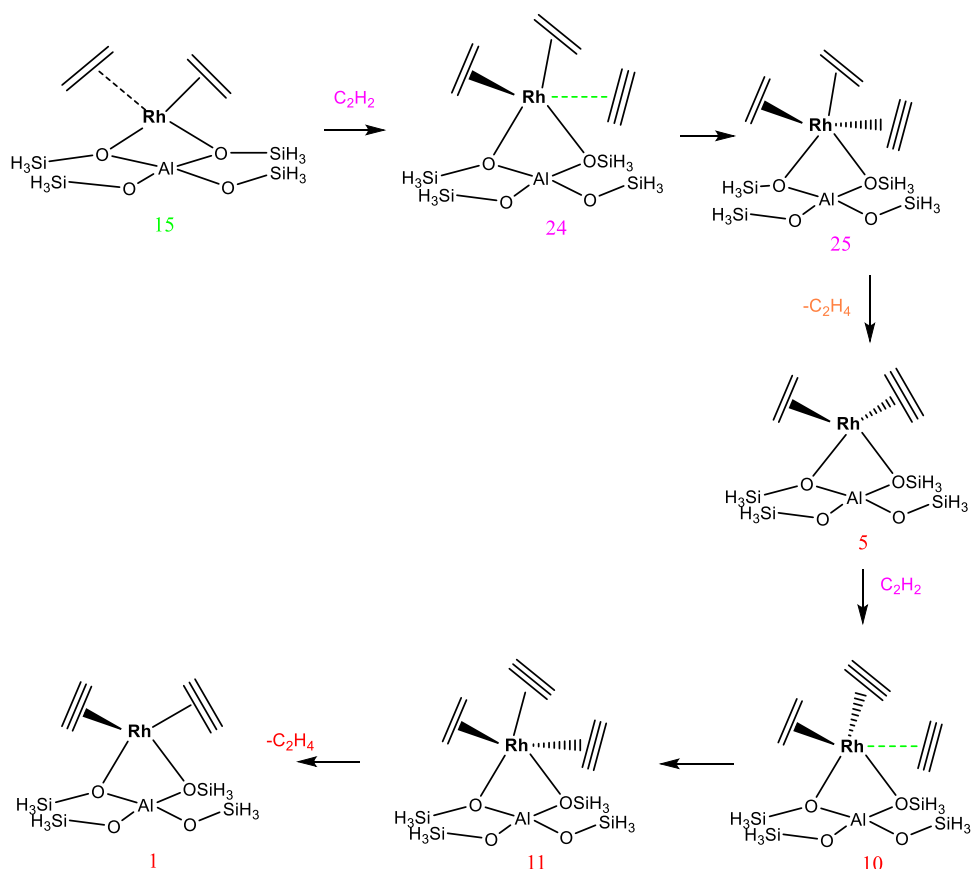
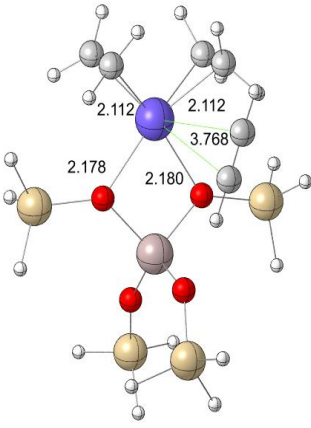
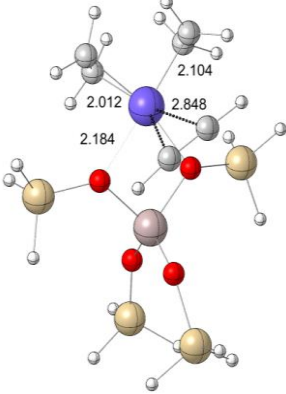
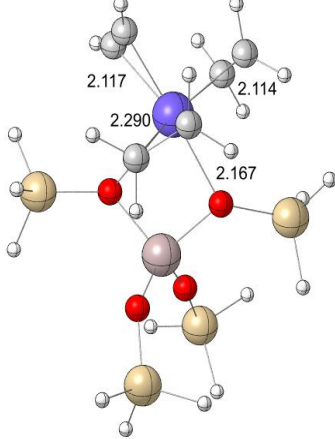
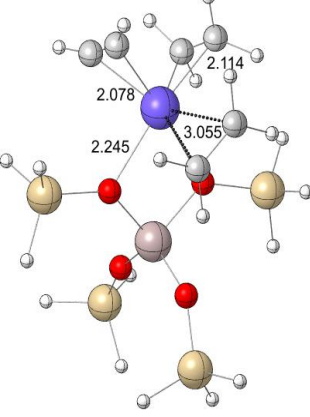


Figure 4.14. 2D mechanism for the replacement of two ethylene groups with acetylene groups on the zeolite supported Rh complexes (Path 2B).

Figure 4.14 explains that the presence of C_2H_2 (acetylene) group can be replaced with the currently found C_2H_4 (ethylene) groups on the Rh metal. The ground and transition state geometries of Path 2B are given in Table 4.10.

Table 4.10. Ground and transition state geometries and bond distances (Å) for Path 2B.

Ground State Geometries	Transition State Geometries
 <p style="text-align: center;">24</p>	 <p style="text-align: center;">TS24-25</p>
 <p style="text-align: center;">25</p>	 <p style="text-align: center;">TS25-5</p>

The PES diagram of Path 2B (15-1) supports the pathway which is given in Figure 4.15. According to this path, C₂H₄ (ethylene) is released easily since it has relatively low (6.3 kcal/mol) activation energy barrier from 25→TS25-5. Total reaction energy is calculated for the replacement of ethylene groups with acetylene groups to be exothermic by -7.8 kcal/mol. The catalyst which is complex 1 is regenerated at the end.

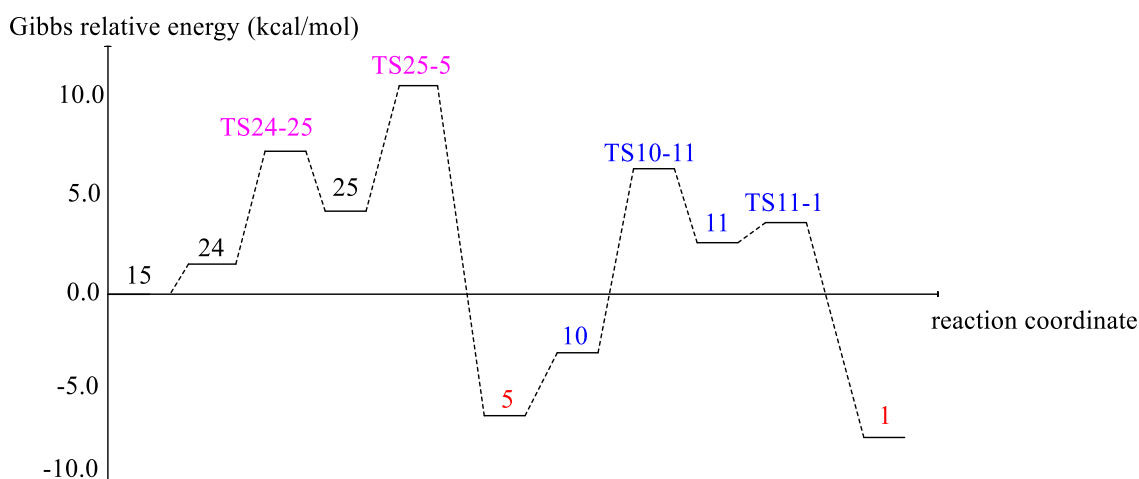


Figure 4.15. Potential energy surface diagram for the regeneration of the catalyst and emission of ethylene (Path 2B).

In addition, when the PES diagrams of Path 2A and Path 2B are compared, it is observed that Path 2B is energetically more favorable than Path 2A by comparing their relative energies. For instance, the activation energy barrier of TS24-25 (6.0 kcal/mol) is lower than the activation energy barrier of TS16-17 (14.5 kcal/mol) or the activation energy barrier of TS25-5 (6.3 kcal/mol) is also lower than the activation energy barrier of TS18-19 (26.0 kcal/mol). Therefore, the ethylene production is selective and reaction pathway prefers to proceed via Path 2B. As a result, catalyst is regenerated and C₂H₄ is emitted from the reactor.

4.3. Comparison of zeolite supported Rh(C₂H₂)₂ and Ir(C₂H₂)₂ catalysts

The catalytic activity and selectivity of ligand binding to the various Group 9 metal complexes can be deduced by comparing them. In this study, the same paths mentioned above are investigated by changing Rh metal with Ir metal. The aim is to observe how the metal change affects the selectivity for the hydrogenation and the regeneration of the catalyst. Therefore, to compare the differences between zeolite supported Rh(C₂H₂)₂ and Ir(C₂H₂)₂ catalysts, bond lengths (metal–ligand (M-C) and metal-oxygen (M-O) distances), ligand bond dissociation energies (LDEs), potential energy surfaces (PESs) and charges on metal are discussed in following sections.

4.3.1. Bond Lengths

In this part of the study, the bond lengths (metal–ligand and metal-oxygen distances) of molecular zeolite-supported site-isolated rhodium and iridium complexes including typical hydrocarbon ligands (C_2H_2 and C_2H_4) are examined by using DFT. The acetylene and ethylene ligands are adsorbed to the Rh and Ir complexes by forming two M-C bonds. In addition, there are two M-O bonds arising from metal and the oxygen atoms at the acidic Al site of zeolite support. The 3D geometries including M-C and M-O distances of complex 1, 5 and 15 for Rh and Ir metals are shown in Figure 4.11. These complexes are chosen to be compared since they have different ligands on the metal. The ordering of M-C bond distance in the all complexes is $d(\text{Ir-C}) < d(\text{Rh-C})$ which as shown in Table 4.12. The stronger Ir-C bonding leads to weaker C-C bonding in the acetylene and ethylene ligands. This means that the Ir complex has a higher effect on the $C\equiv C$ triple bond and $C=C$ double bond in acetylene and ethylene than the Rh complexes. The ordering of M-O bond distance in the all complexes is $d(\text{Ir-O}) < d(\text{Rh-O})$ which is also given in Table 4.12. Moreover, it is observed that the strength of M(Rh/Ir)-C bonds decreases or the length of M(Rh/Ir)-C bonds increases for complex 1, 5 and 15 as the ligand changes from C_2H_2 to C_2H_4 . Strong π -donor ligands like CH_3CH_3 , C_2H_6 , and C_2H_2 can improve back-bonding between molecules [112].

In terms of comparing experimental data and computations, Uzun *et al.* have provided numerous good examples. They presented findings from several studies on the structure and catalytic characteristics of atomically distributed iridium on zeolite. According to the EXAFS data, each Ir atom was bonded to four carbon atoms at an average distance of 2.10 Å, which is compatible with the existence of two ethylene ligands per Ir atom and with the IR spectra confirming π -bonded ethylene ligands. The EXAFS results further show that each Ir atom was bound to two oxygen atoms of the zeolite at a distance of 2.15 Å [113]. The observed and computed results were found to be in good agreement for zeolite supported $\text{Ir}(C_2H_4)_2$ which are shown in Table 4.12.

Table 4.11. 3D geometries of complex 1, 5 and 15 with M-C and M-O bond distances (Å).

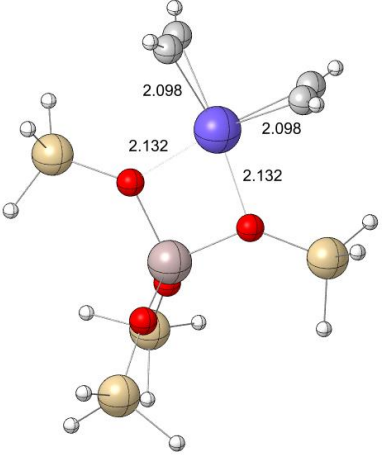
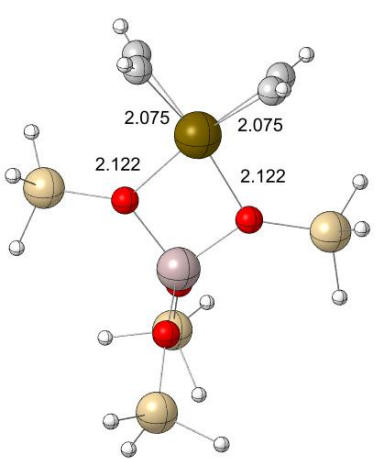
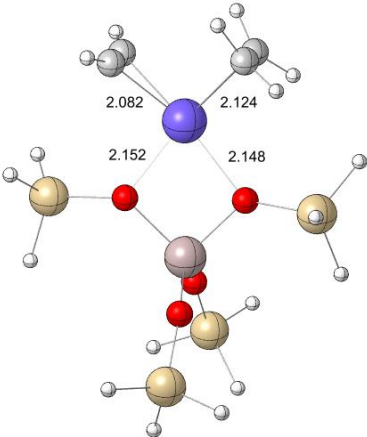
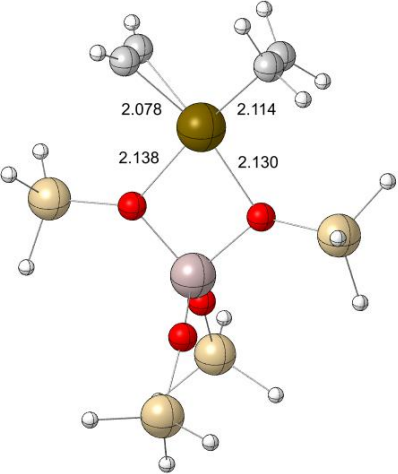
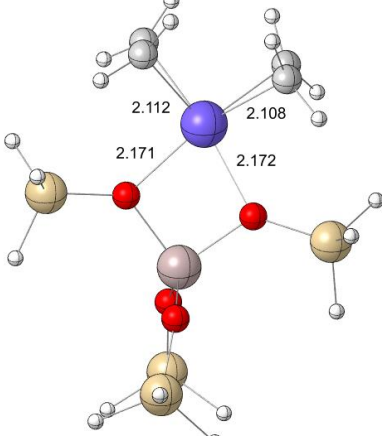
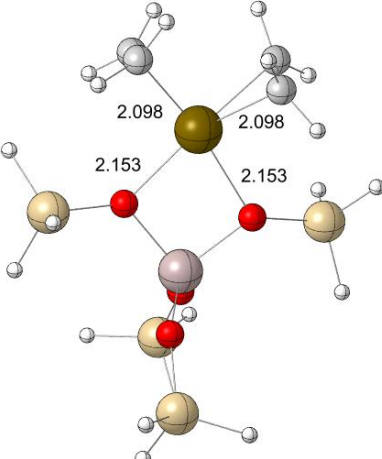
M = Rh	M = Ir
 <p data-bbox="582 927 598 958">1</p>	 <p data-bbox="1102 927 1150 958">1-Ir</p>
 <p data-bbox="582 1480 598 1512">5</p>	 <p data-bbox="1102 1480 1150 1512">5-Ir</p>
 <p data-bbox="574 1995 608 2027">15</p>	 <p data-bbox="1094 1995 1158 2027">15-Ir</p>

Table 4.12. M-C and M-O bond distances (Å) for complexes 1, 5 and 15.

Ligand(s)	M = Rh		M = Ir	
	d(M-C)	d(M-O)	d(M-C)	d(M-O)
C ₂ H ₂ /C ₂ H ₂ (1)	2.098, 2.098	2.132	2.075, 2.075	2.122
C ₂ H ₂ /C ₂ H ₄ (5)	2.082, 2.124	2.150	2.078, 2.114	2.134
C ₂ H ₄ /C ₂ H ₄ (15)	2.108, 2.112	2.172	2.098, 2.098	2.153

Table 4.13. C-C triple and double bond lengths (Å) for complexes 1, 5 and 15.

Ligand(s)	M = Rh		M = Ir	
	d(C≡C)	d(C=C)	d(C≡C)	d(C=C)
C ₂ H ₂ /C ₂ H ₂ (1)	1.266	-	1.276	-
C ₂ H ₂ /C ₂ H ₄ (5)	1.269	1.414	1.279	1.428
C ₂ H ₄ /C ₂ H ₄ (15)	-	1.418		1.432

The C-C triple and double bond distances in the ligands for complex 1, 5 and 15 for Rh and Ir metals are shown in Table 4.13. It is observed that as the hydrogenation mechanism proceeds that is C₂H₂ ligand turns into C₂H₄, C≡C triple bond and C=C double bond elongate. Since π back donation from metal to ligand increases p character, it weakens the bond strength. Moreover, it is seen that this donation is stronger for Ir since C-C triple and double bonds in ligands are longer for Ir than Rh.

4.3.2. Ligand Bond Dissociation Energies (LDEs)

The energy required to break a chemical bond is known as *bond dissociation energy*. It's a way of measuring the strength of a chemical bond [114]. Since ligands (C₂H₂ and C₂H₄) on the metal are used in this study, ligand bond dissociation energies are reported.

To calculate the LDEs, complex 5 is chosen for Rh and Ir complexes since it has both acetylene and ethylene ligands on the metal. The LDE calculation is carried out by scanning the distance between M(Rh/Ir) and C ligand (C_2H_2 / C_2H_4) by 0.5 Å in each step starting from the structure corresponding to the global minimum. The difference between the initial and final electronic energies are calculated. The LDEs have been determined as shown in Table 4.14 and the electronic energies versus M-C distances are illustrated in Figure 4.16-4.19.

Table 4.14. Ligand bond dissociation energies (kcal/mol) of complex 5 for Rh and Ir complexes

Metal Complex	LDE(C_2H_2)	LDE(C_2H_4)
Rh(C_2H_2)(C_2H_4)	62.4	57
Ir(C_2H_2)(C_2H_4)	83.8	74.9

According to Table 4.13, the results imply that C_2H_2 ligand is more strongly bonded for the Rh or Ir complexes because the energy to dissociate the M- C_2H_2 bond is relatively high compared to C_2H_4 ligand. This outcome also overlaps with the bond length results in Section 4.3.1. The bond length of M- C_2H_2 ligand is shortest, thus it is stronger bond compared to others. In addition, it is seen that C_2H_2 ligand is more strongly bonded to Ir metal (21.4 kcal/mol higher) than Rh metal. This case is also valid for C_2H_4 ligand. The LDE of C_2H_4 for Ir is 17.9 kcal/mol greater than for Rh. The C_2H_4 ligand is more bent out of plane compared to C_2H_2 . The Ir- C_2H_4 distortion reduces the overlap between the Ir and C=C electron densities, lowering the C_2H_4 bond energy. Although C_2H_2 is a η^2 bonding ligand, the steric effect of Ir(C_2H_2) supported on zeolite is relatively low. The ordering of the LDEs for Rh and Ir is significant in predicting the selectivity of catalytic reactions, especially in hydrocarbon activation processes where the reaction kinetics of the intermediate ligand complexes are important.

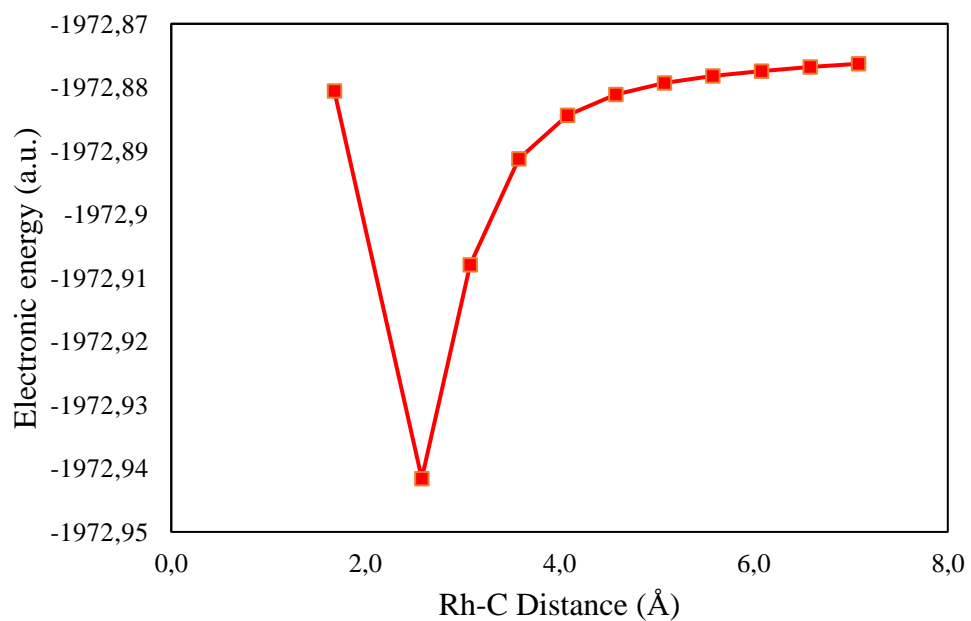


Figure 4.16. Ligand bond dissociation energy for C₂H₂ in the Rh(C₂H₂)(C₂H₄) complex.

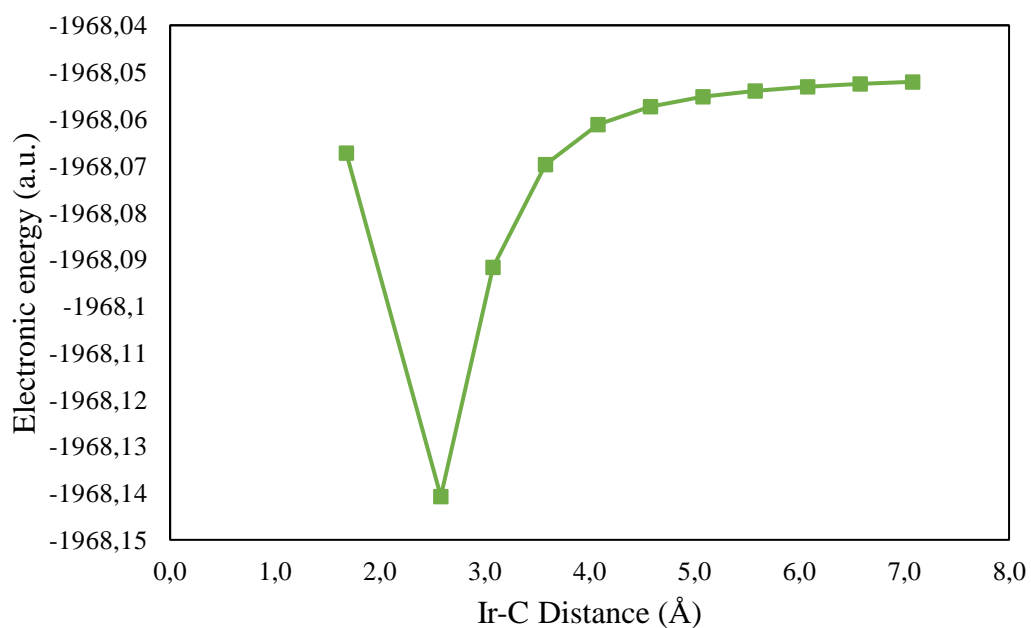


Figure 4.17. Ligand bond dissociation energy for C₂H₂ in the Ir(C₂H₂)(C₂H₄) complex.

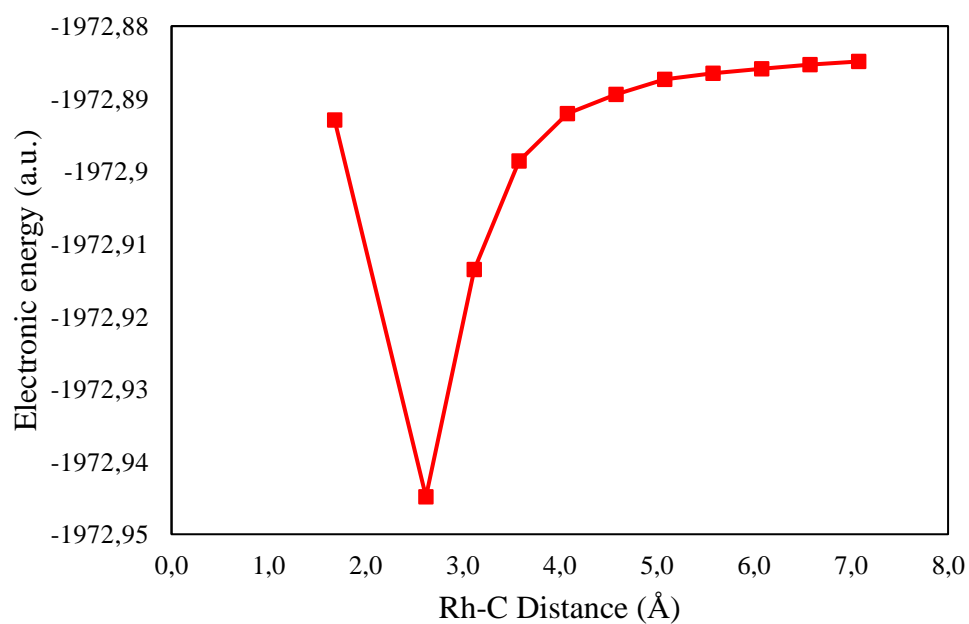


Figure 4.18. Ligand bond dissociation energy for C₂H₄ in the Rh(C₂H₂)(C₂H₄) complex.

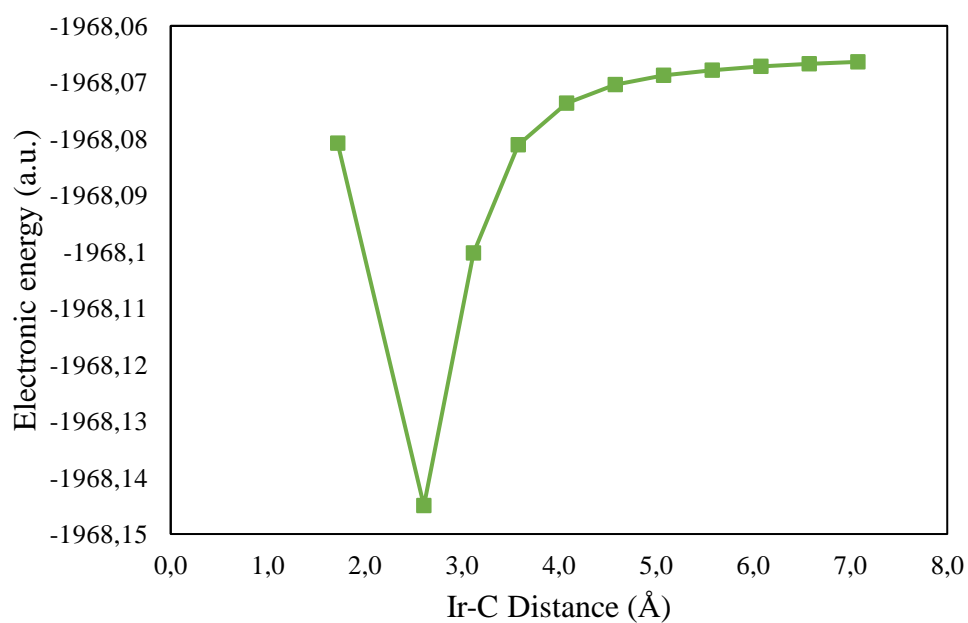


Figure 4.19. Ligand bond dissociation energy for C₂H₄ in the Ir(C₂H₂)(C₂H₄) complex.

4.3.3. Potential Energy Surfaces

In this section, the comparison of the theoretically calculated potential energy surfaces (PESs) of paths using zeolite supported Rh and Ir catalysts are investigated. The variations in the stabilities of the intermediates on the PES's for $M = \text{Rh}$ and Ir result in significantly different energetics for the C_2H_2 and C_2H_4 hydrogenation reaction on these M -zeolite catalysts. The PES diagram of the hydrogenation for $\text{Rh}(\text{C}_2\text{H}_2)_2$ and $\text{Ir}(\text{C}_2\text{H}_2)_2$ catalysts with 2D structures of each complex with relative Gibbs free energies (kcal/mol) are represented in Figure 4.20 and Figure 4.21. Potential energy surface diagrams are represented in Table 4.15 and Table 4.16. According to these PESs, it is obvious to comprehend the relatively small barriers of Ir (green) compared to Rh (red). This situation is also mimicked for the hydrogenation for $\text{Rh}(\text{C}_2\text{H}_4)_2$ and $\text{Ir}(\text{C}_2\text{H}_4)_2$ (Table 4.17). The zeolite-supported iridium complex's catalytic activity was found to be approximately 35 times higher than that of the similar rhodium complex [113]. On the contrary, the regeneration of catalysts and the emission of C_2H_4 and C_2H_6 is facile with Rh . The PES diagrams are represented in Figure 4.23, Figure 4.24 and Figure 4.25. 2D structures with relative energies are given in Table 4.18 and Table 4.19.

Table 4.15. 2D structures of each complex with relative Gibbs free energies (Path 1).

	1	2	TS2-3	3	TS3-4	4	TS4-5	5
M = Rh	0.00	5.08	26.0	18.2	18.5	-1.87	20.6	0.51
M = Ir		5.07	19.5	3.39	8.07	1.73	11.5	1.38

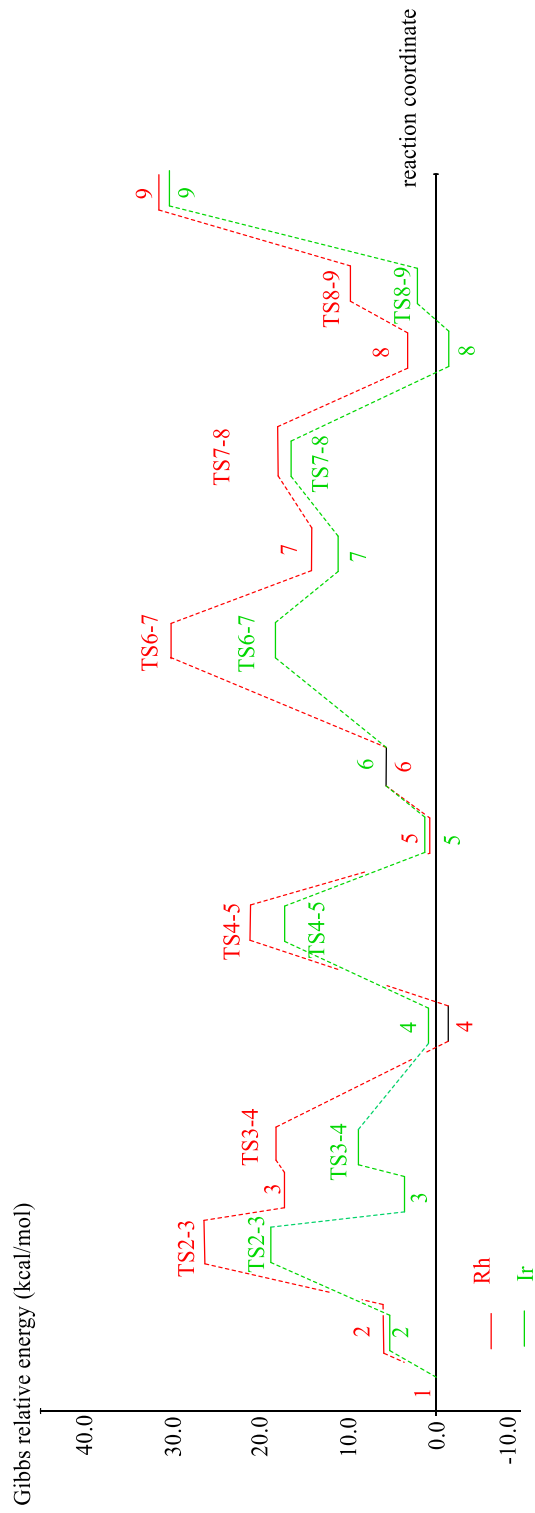


Figure 4.20. Potential energy surface diagram for the acetylene hydrogenation of zeolite-supported Rh(C₂H₂)₂ and Ir(C₂H₂)₂ complexes (Path 1).

Table 4.16. 2D structures of each complex with relative Gibbs free energies (Path 1).

	6	TS6-7	7	TS7-8	8	TS8-9	9
M = Rh	5.41	30.8	14.1	18.4	9.03	37.7	32.7
M = Ir	6.04	19.8	10.4	17.3	-1.40	34.4	30.4

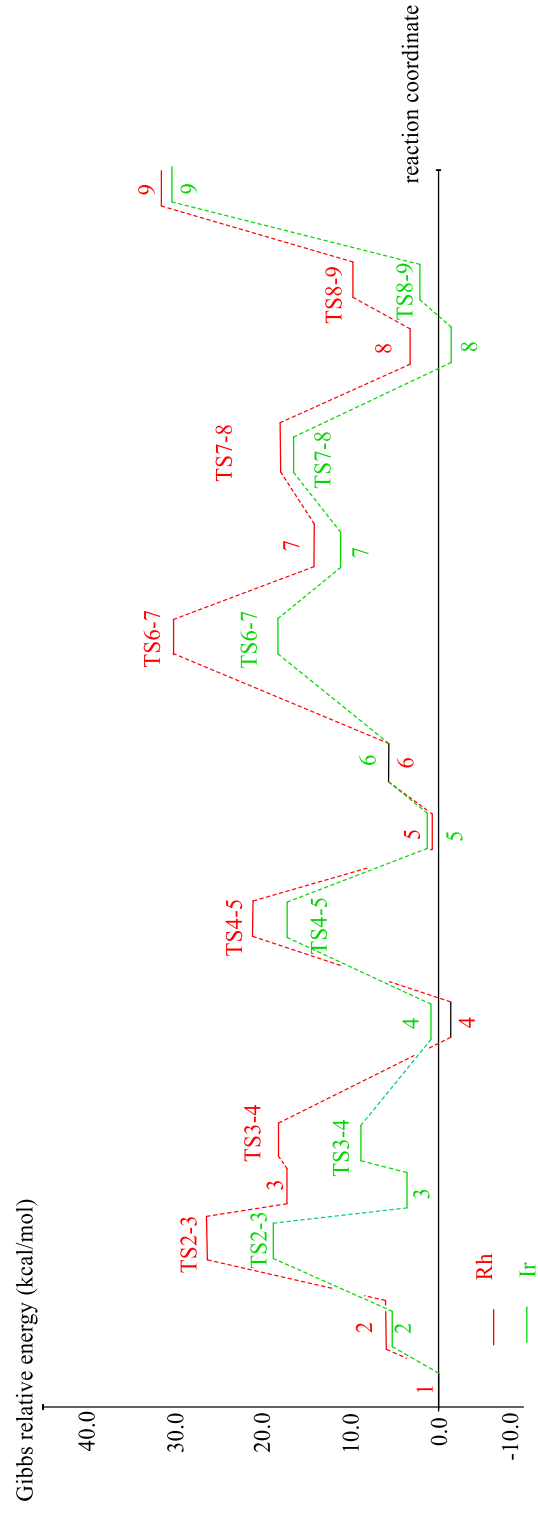
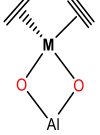
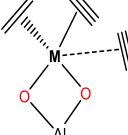
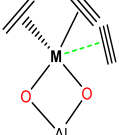
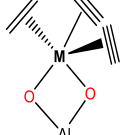
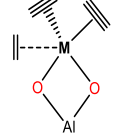
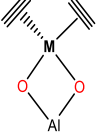
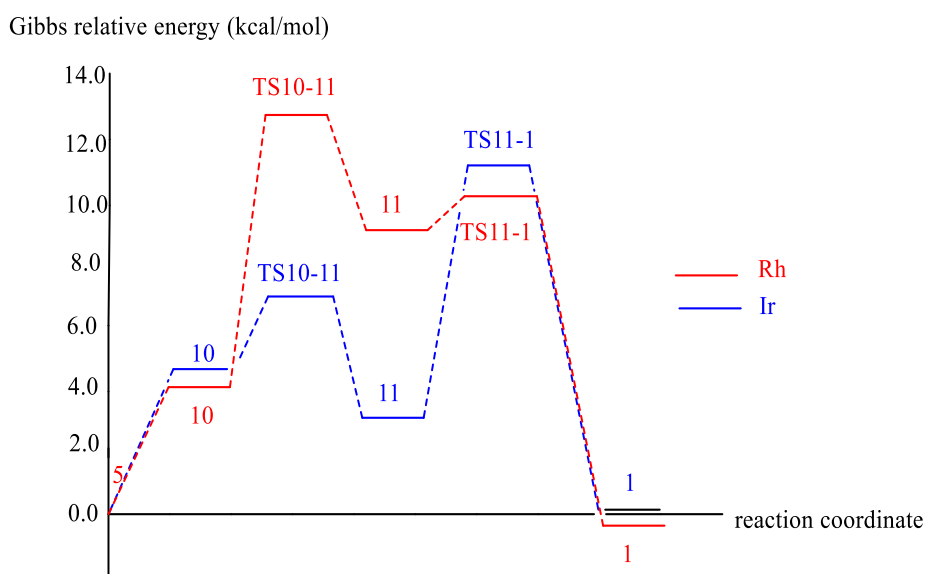


Figure 4.21. Potential energy surface diagram for the acetylene hydrogenation of zeolite-supported $\text{Rh}(\text{C}_2\text{H}_2)_2$ and $\text{Ir}(\text{C}_2\text{H}_2)_2$ complexes (Path 1).

Table 4.18. 2D structures of each complex with relative Gibbs free energies (Path 1A).

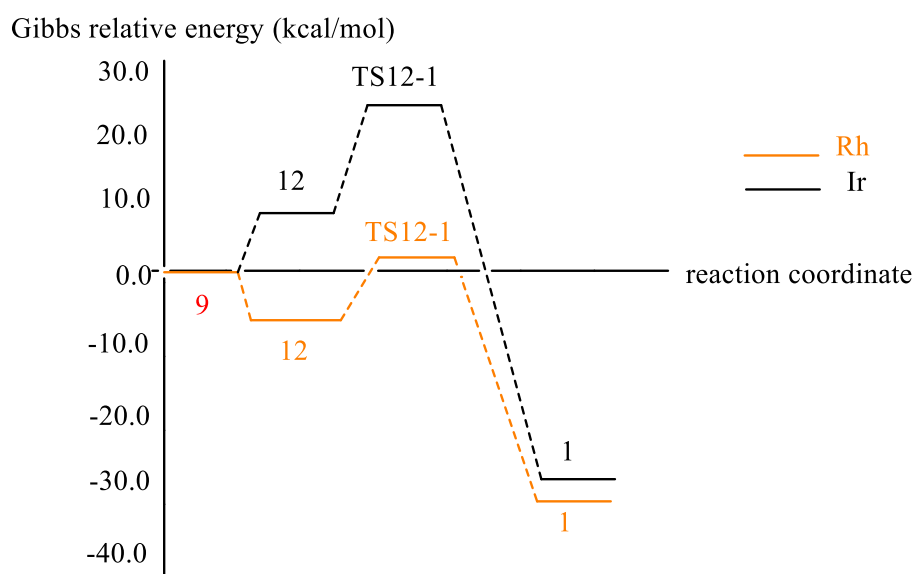
	5	10	TS10-11	11	TS11-1	1
M = Rh						
M = Ir	0.0	4.02	12.7	9.36	10.1	-0.51
		4.49	7.62	3.01	11.3	-0.93

Figure 4.23. Potential energy surface diagram for the regeneration of zeolite-supported Rh(C₂H₂)(C₂H₄) and Ir(C₂H₂)(C₂H₄) complexes (Path 1A).

According to Table 4.18, for Ir, the rate of reaction is controlled by the last stage of the catalytic cycle (11 → TS11-1), the production and release of C₂H₄. The PES reaction for Ir reveals that the intermediates are extremely stable, implying that removing the C₂H₄ is significantly more difficult. While the activation energy barrier (11 → TS11-1) for Rh is 0.7 kcal/mol, the activation energy barrier (11 → TS11-1) for Ir is 8.3 kcal/mol.

Table 4.19. 2D structures of each complex with relative Gibbs free energies (Path 1B).

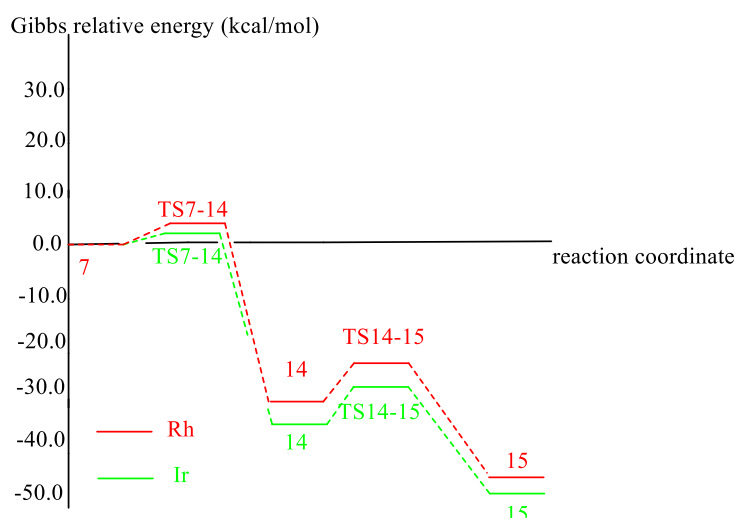
	9	12	TS12-1	1
M = Rh	0.0	-7.25	1.61	-32.7
M = Ir		9.16	28.0	-30.4

Figure 4.24. Potential energy surface diagram for the regeneration of zeolite-supported $\text{Rh}(\text{C}_2\text{H}_2)(\text{C}_2\text{H}_6)$ and $\text{Ir}(\text{C}_2\text{H}_2)(\text{C}_2\text{H}_6)$ complexes (Path 1B).

Similarly, in Table 4.19 from Ir to Rh, the energy required to release C_2H_6 declines as a result of the stability of the intermediates. While the activation energy barrier ($12 \rightarrow \text{TS12-1}$) for Rh is 8.86 kcal/mol, the energy required to release C_2H_6 ($12 \rightarrow \text{TS12-1}$) for Ir is 19.2 kcal/mol.

Table 4.20. 2D structures of each complex with relative Gibbs free energies (Path 2).

	7	TS7-14	14	TS14-15	15
M = Rh	0.0	4.1	-30.1	-24.4	-48.1
M = Ir	0.0	0.7	-32.6	-26.3	-47.0

Figure 4.25. Potential energy surface diagram for the acetylene hydrogenation of zeolite-supported $\text{Rh}(\text{C}_2\text{H}_2)(\text{C}_2\text{H}_4)$ and $\text{Ir}(\text{C}_2\text{H}_2)(\text{C}_2\text{H}_4)$ complexes (Path 2).

The PES diagram of the hydrogenation for $\text{Rh}(\text{C}_2\text{H}_2)(\text{C}_2\text{H}_4)$ and $\text{Ir}(\text{C}_2\text{H}_2)(\text{C}_2\text{H}_4)$ complexes with 2D structures and relative Gibbs free energies (kcal/mol) are represented in Table 4.20. Likewise the hydrogenation mechanisms of Path 1 and Path 2A, the relatively small barriers of Ir (green) compared to Rh (red) are observed. As the calculated LDE results in Section 4.3.2 indicate, Ir makes the stronger M- C_2H_4 bonds compared to Rh. The stronger Ir-C bonds substantially weaken the C=C and C \equiv C bonds. This infers two meanings in the catalysis of the acetylene and ethylene hydrogenation reactions. One of these meaning is that the adsorbed acetylene or ethylene can be most extensively activated by the Ir catalyst. Therefore, the hydrogenation mechanisms are facile with Ir. The other meaning is that the release of the hydrogenation product C_2H_4 and C_2H_6 is more challenging for the Ir catalyst. For ethylene hydrogenation processes, the Ir catalyst performs better than the Rh catalyst experimentally [112].

4.3.4. Charges on Metal

Charge analysis was carried out using charge model 5 (CM5). The charges on metals are given in Table 4.20. For Path 1, Rh metal is more positively charged than Ir. It is logical since Ir has more electron and these electrons are close to the surface due to the screening effect. Because Ir has f orbitals which are weakly attracted to the nucleus, they are unable to shield the nucleus, resulting in a poor shielding effect. Moreover, this effect can explain the convenience of hydrogenation reaction. The metal (Rh or Ir) for complex 4 in Path 1 has the most positive charge and has less electrons on the surface. The metal (Rh or Ir) for complex 9 has negative charge meaning to has more electron on it since the one of the ligands on the metal is C₂H₆.

Table 4.21. CM5 charges on metal for the hydrogenation of Rh(C₂H₂)₂ and Ir(C₂H₂)₂ complexes (Path 1).

PATH 1		
Molecule ID	Charge on Rh	Charge on Ir
1	0.5336	0.4801
2	0.5329	0.4806
3	0.4375	0.4235
4	0.5608	0.4952
5	0.5361	0.4842
6	0.5352	0.4843
7	0.5255	0.4885
8	0.5020	0.4613
9	0.4369	0.3619

Table 4.22. CM5 charges on metal for the regeneration of Rh(C₂H₂)₂ and Ir(C₂H₂)₂ complexes (Path 1A).

Path 1A		
Molecule ID	Charge on Rh	Charge on Ir
5	0.5361	0.4842
10	0.5313	0.4823
11	0.5729	0.5665
1	0.5336	0.4801

Table 4.23. CM5 charges on metal for the regeneration of $\text{Rh}(\text{C}_2\text{H}_2)_2$ and $\text{Ir}(\text{C}_2\text{H}_2)_2$ complexes (Path 1B).

Path 1B		
Molecule ID	Charge on Rh	Charge on Ir
9	0.4369	0.3619
12	0.4821	0.3873
1	0.5336	0.4801

According to Table 4.21, the same trend (Rh is more positively charged than Ir) is observed. These paths (Path 1A and Path 1B) refer to the emission of C_2H_4 and C_2H_6 , respectively. For Path 1A, Rh and Ir is more positively charged when the metal is in complex 11. This complex has three ligands ($2\text{C}_2\text{H}_2 + \text{C}_2\text{H}_4$) on the metal. For Path 1B, complex 1 is most positively charged among complex 9 and 12 since while they have ethane and acetylene groups on the metal, complex 1 has only 2 acetylene groups on the metal which are given in Table 4.22.

5. CONCLUSION

In the first part of the thesis, the hydrogenation reaction mechanism of Rh complexes bonded to zeolite support are investigated by modeling the pathways. These paths include zeolite supported $\text{Rh}(\text{C}_2\text{H}_2)_2$ hydrogenation, the regeneration of the catalyst and the comparisons of the two. It is concluded that, for Path 1, ethylene production is more selective than ethane production since the activation energy barrier from ethylene to ethane is relatively high. The regeneration of the catalyst as well as the emission of C_2H_4 (ethylene) via the reaction mechanism Path 1A are also investigated and this path is more favorable than Path 1. If the C_2H_6 (ethane) is released at the end of the hydrogenation reaction (Path 1); it is easy to regenerate the catalyst via Path 1B. Moreover, the production of $\text{Rh}(\text{C}_2\text{H}_4)_2$ is preferred rather than the $\text{Rh}(\text{C}_2\text{H}_2)(\text{C}_2\text{H}_6)$ and as the $\text{Rh}(\text{C}_2\text{H}_4)_2$ is hydrogenated (Path 2A), it is observed that two ethylene groups on Rh cannot form two ethane groups, but the catalyst is again regenerated in Path 2B.

In the second part of the thesis, the Rh metal is replaced with Ir metal to see the influences of metal on the selectivity for hydrogenation and catalyst regeneration. When the metal is Ir instead of Rh metal, the hydrogenation mechanism is facile as observed from the activation energy barriers; however, the regeneration of the catalyst is more likely to occur with Rh metal. The difference in activity arises from the ligand bond dissociation energies (LDEs). Higher LDEs are calculated for Ir metal for the dissociation of ligands (C_2H_2 and C_2H_4). LDE is associated to the electron density distribution in the ligand. Correspondingly, bond lengths (metal-ligand and metal-oxygen) are shorter with Ir metal. Rh metal has more positively charged than Ir owing to the screening effect of f orbitals. Because of the poor shielding, these electrons are near to the surface and f orbitals are weakly attached to the nucleus, thus they can't shelter the nucleus.

Overall, the choice of metal and additional ligands can improve the reactivity of the catalyst. The catalytic activity and confinement effects are not fully reflected by small cluster models of zeolites.

Larger supports can be used to confirm the results or supports having different electron donor/acceptor properties such as MgO, SiO₂, La₂O₃, Fe₂O₃, TiO₂ can be used to tune the catalytic properties.

Newly emergent SACs also contribute to the development of the hydrogenation reactions. The metals different from single Rh and Ir atoms can be good candidates for further applications. The computational results, together with the experimental observations, are expected to a better view of the catalytic hydrogenation of acetylene and ethylene on single site supported Rh and Ir catalysts, as well as suggestions for future experimental investigations.

REFERENCES

1. Vallianatou, K. A., D. J. Frank, G. Antonopoulou, S. Georgakopoulos, E. Siapi, and M. Zervou, "Rhodium-Catalyzed Asymmetric Olefin Hydrogenation by Easily Accessible Aniline and Pyridine-derived Chiral Phosphites," *Tetrahedron Letters*, vol. 54, no. 5, pp. 397–401, 2013.
2. Hoelscher, H. E., W. G. Poynter, and E. Weger, "The Vapor-Phase Catalytic Hydrogenation of Olefins.," *Chemical Reviews*, vol. 54, no. 4, pp. 575–592, 1954.
3. Bianchini, C., A. Meli, M. Peruzzini, P. Frediani, C. Bohanna, and M. A. Esteruelas, "Selective Hydrogenation of 1-alkynes to Alkenes Catalyzed by an iron(II) cis-hydride η^2 -dihydrogen complex. a Case of Intramolecular Reaction between η^2 -H₂ and s-Vinyl Ligands," *Organometallics*, vol. 11, no. 1, pp. 138–145, 1992.
4. Schleyer, D., H. G. Niessen, and J. Bargon, "In Situ 1h-Phip-Nmr Studies of the Stereoselective Hydrogenation of Alkynes to (E)-Alkenes Catalyzed by a Homogeneous [Cp*Ru]⁺ Catalyst," *New Journal of Chemistry*, vol. 25, no. 3, pp. 423–426, 2001.
5. Navarro, J., M. Sági, E. Sola, F. J. Lahoz, T. Dobrinovitch, and Á. Kathó, "Unusual 1-Alkyne Dimerization/Hydrogenation Sequences Catalyzed by [Ir(H)₂(NCCH₃)₃(P-i-Pr₃)]BF₄: Evidence for Homogeneous-Like Mechanism in Imidazolium Salts," *Advanced Synthesis & Catalysis*, vol. 345, no. 12, pp. 280–288, 2003.
6. Costa, N.J.S., L.M. Rossi, "Synthesis of Supported Metal Nanoparticle Catalysts Using Ligand Assisted Methods", *Nanoscale*, vol. 4, pp. 5826–5834, 2012.
7. Article, E., M. Babucci, C. Fang, J.E. Perez-aguilar, S. Ho, A. Boubnov, E. Guan, S.R. Bare, and C. Gates, "Controlling Catalytic Activity and Selectivity for Partial Hydrogenation by Tuning the Environment Around Active Sites in Iridium Complexes Bonded to Supports", *Chemical Science*, vol. 10, pp. 2623–2632, 2019.

8. Chen, G., C. Xu, X. Huang, “Interfacial Electronic Effects Control the Reaction Selectivity of Platinum Catalysts”, *Nature Materials*, vol. 15, pp. 564–569, 2016.
9. Lee, I., F. Delbecq, R. Morales, “Tuning Selectivity in Catalysis by Controlling Particle Shape”, *Nature Materials*, vol. 8, pp.132–138, 2019.
10. Reske, R., H. Mistry, F. Behafarid, “Particle Size Effects in The Catalytic Electroreduction of CO₂ on Cu Nanoparticles”, *Journal of the American Chemical Society*, vol. 136, pp. 6978–6986, 2014.
11. Chai, Y., G. Wu, X. Liu, Y. Ren, W. Dai, and C. Wang, “Acetylene-Selective + Hydrogenation Catalyzed by Cationic Nickel Confined in Zeolite,” *Journal of the American Chemical Society*, vol. 141, no. 25, pp. 9920–9927, 2019.
12. Studt, F., F. Abild-Pedersen, T. Bligaard, R. Z. Sorensen, C. H. Christensen, and J. K. Norskov, “Identification of Non-Precious Metal Alloy Catalysts for Selective Hydrogenation of Acetylene,” *Science*, vol. 320, no. 5881, pp. 1320–1322, 2008.
13. Lv, C. Q., J. H. Liu, Y. Guo, and G. C. Wang, “Selective Hydrogenation of 1,3-Butadiene Over Single Pt1/Cu(1 1 1) Model Catalysts: A Dft Study,” *Applied Surface Science*, vol. 466, pp. 946–955, 2019.
14. Chai, Y., G. Wu, X. Liu, Y. Ren, W. Dai, and C. Wang, “Acetylene-Selective Hydrogenation Catalyzed by Cationic Nickel Confined in Zeolite,” *Journal of the American Chemical Society*, vol. 141, no. 25, pp. 9920–9927, 2019.
15. Rao, D. M., T. Sun, Y.S. Yang, P. Yin, M. Pu, and H. Yan, “Theoretical Study on the Reaction Mechanism and Selectivity of Acetylene Semi-Hydrogenation on Ni–Sn Intermetallic Catalysts,” *Physical Chemistry Chemical Physics*, vol. 21, no. 3, pp. 1384–1392, 2019.

16. Van Santen, R. A., G. J. Kramer, "Reactivity Theory of Zeolitic Brønsted Acidic Sites," *Chemical Reviews*, vol. 95, no. 3, pp. 637–660, 1995.
17. Degnan, T. F., "The Implications of The Fundamentals of Shape Selectivity for the Development of Catalysts for the Petroleum and Petrochemical Industries," *Journal of Catalysis*, vol. 216, no. 1–2, pp. 32–46, 2003.
18. Yu, M., R. D. Noble, J. L. Falconer, "Zeolite Membranes: Microstructure Characterization and Permeation Mechanisms," *Accounts of Chemical Research*, vol. 44, no. 11, pp. 1196–1206, 2011.
19. Serrano, D. P., J. M. Escola, P. Pizarro, "Synthesis Strategies in the Search for Hierarchical Zeolites," *Chemical Society Reviews*, vol. 42, no. 9, pp. 4004–4035, 2013.
20. Kubička, D., I. Kubičková, J. Čejka, "Application of Molecular Sieves in Transformations of Biomass and Biomass-Derived Feedstocks," *Catalysis Reviews*, vol. 55, no. 1, pp. 1–78, 2013.
21. Speybroeck, V. V., K. Hemelsoet, L. Joos, M. Waroquier, R. G. Bell, and C. R. A. Catlow, "Advances in Theory and Their Application Within the Field of Zeolite Chemistry," *Chemical Society Reviews*, vol. 44, no. 20, pp. 7044–7111, 2015.
22. Lukyanov, D. B., S. J. Beckett, T. Vazhnova, "Toward Better Understanding of the Catalytic Action of Acidic Zeolites: Investigation in Methane and Ethane Activation and Transformation," *ACS Catalysis*, vol. 2, no. 12, pp. 2596–2601, 2012.
23. Olsbye, U., S. Svelle, M. Bjørgen, P. Beato, T. V. W. Janssens, and F. Joensen, "Conversion of Methanol to Hydrocarbons: How Zeolite Cavity and Pore Size Controls Product Selectivity," *Angewandte Chemie International Edition*, vol. 51, no. 24, pp. 5810–5831, 2012.

24. Mlinar, A. N., P. M. Zimmerman, F. E. Celik, M. Head-Gordon, and A. T. Bell, "Effects of Brønsted-Acid Site Proximity on the Oligomerization of Propene in H-Mfi," *Journal of Catalysis*, vol. 288, pp. 65–73, 2012.
25. Van der Mynsbrugge, J., M. Visur, U. Olsbye, P. Beato, M. Bjørgen, and V. Van Speybroeck, "Methylation of Benzene by Methanol: Single-Site Kinetics over H-Zsm-5 and H-Beta Zeolite Catalysts," *Journal of Catalysis*, vol. 292, pp. 201–212, 2012.
26. Serna, P., B. C. Gates, "A Bifunctional Mechanism for Ethene Dimerization: Catalysis by Rhodium Complexes on Zeolite HY in the Absence of Halides," *Angewandte Chemie International Edition*, vol. 50, no. 24, pp. 5528–5531, 2011.
27. Serna, P., B. C. Gates, "Zeolite-Supported Rhodium Complexes and Clusters: Switching Catalytic Selectivity by Controlling Structures of Essentially Molecular Species," *Journal of the American Chemical Society*, vol. 133, no. 13, pp. 4714–4717, 2011.
28. Bakowies D., W. Thiel, "Hybrid Models for Combined Quantum Mechanical and Molecular Mechanical Approaches," *The Journal of Physical Chemistry*, vol. 100, no. 25, pp. 10580–10594, 1996.
29. Nasluzov, V. A., E. A. Ivanova, A. M. Shor, G. N. Vayssilov, U. Birkenheuer, and N. Rösch, "Elastic Polarizable Environment Cluster Embedding Approach for Covalent Oxides and Zeolites Based on a Density Functional Method," *The Journal of Physical Chemistry B*, vol. 107, no. 10, pp. 2228–2241, 2003.
30. Kletnieks, P. W., A. J. Liang, R. Craciun, J.O. Ehresmann, D.M. Marcus, and V.A. Bhirud, "Molecular Heterogeneous Catalysis: A Single-Site Zeolite-Supported Rhodium Complex for Acetylene Cyclotrimerization," *Chemistry - A European Journal*, vol. 13, no. 26, pp. 7294–7304, 2007.

31. De Moor, B. A., M.F. Reyniers, M. Sierka, J. Sauer, and G. B. Marin, “Physisorption and Chemisorption of Hydrocarbons in H-FAU Using QM-Pot(MP2//B3LYP) Calculations,” *The Journal of Physical Chemistry C*, vol. 112, no. 31, pp. 11796–11812, 2008.
32. Maihom, T., B. Boekfa, J. Sirijaraensre, T. Nanok, M. Probst, and J. Limtrakul, “Reaction Mechanisms of the Methylation of Ethene with Methanol and Dimethyl Ether over H-ZSM-5: An ONIOM Study,” *The Journal of Physical Chemistry C*, vol. 113, no. 16, pp. 6654–6662, 2009.
33. Boscoboinik, J. A., X. Yu, B. Yang, F. D. Fischer, R. Włodarczyk, and M. Sierka, “Modeling Zeolites with Metal-Supported Two-Dimensional Aluminosilicate Films,” *Angewandte Chemie International Edition*, vol. 51, no. 24, pp. 6005–6008, 2012.
34. Hemelsoet, K., J. Mynsbrugge, K. D. Wispelaere, M. Waroquier, and V. Van Speybroeck, “Unraveling the Reaction Mechanisms Governing Methanol-to-Olefins Catalysis by Theory and Experiment,” *ChemPhysChem*, vol. 14, no. 8, pp. 1526–1545, 2013.
35. Markova, V. K., G. N. Vayssilov, N. Rösch, “Hydrogen Adsorption on Small Zeolite-Supported Rhodium Clusters. A Density Functional Study,” *The Journal of Physical Chemistry C*, vol. 119, no. 2, pp. 1121–1129, 2014.
36. Born, M., R. Oppenheimer, “Zur Quantentheorie der Molekeln”, *Annalen der Physik*, vol. 389, no. 20, pp. 457–484, 1927.
37. Engel, E., R. M. Dreizler, *Density Functional Theory Theoretical and Mathematical Physics*, Springer-Verlag Berlin Heidelberg, 2011.
38. Becke, A. D., “A new mixing of Hartree–Fock and local density functional theories”, *The Journal of Chemical Physics*, vol. 98, no. 2, pp. 1372–1377, 1993.

39. Becke, A. D., “Density Functional Exchange Energy Approximation with Correct Asymptotic Behavior”, *Physical Review A*, vol. 38, pp. 3098–3100, 1988.
40. Hohenberg, P., W. Kohn, “Inhomogeneous Electron Gas”, *Physical Review*, vol. 136, pp. B864–B871, 1964.
41. Kohn, W., L. J. Sham, “Self-Consistent Equations Including Exchange and Correlation Effects”, *Physical Review*, vol. 140, no. 4A, pp. A1133–A1138, 1965.
42. Perdew, J. P., J. A. Chevary, S. H. Vosko, K. A. Jackson, M. R. Pederson, and D. J. Singh, “Atoms, molecules, solids, and surfaces: Applications of the Generalized Gradient Approximation for Exchange and Correlation,” *Physical Review B*, vol. 46, no. 11, pp. 6671–6687, 1992.
43. Perdew, J. P., K. Burke, M. Ernzerhof, “Generalized Gradient Approximation Made Simple”, *Physical Review Letters*, vol. 77, pp. 3865–3868, 1996.
44. Curtiss, L. A., P. C. Redfern, K. Raghavachari, “Assessment of Gaussian-3 and Density Functional Theories on the G3/05 Test Set of Experimental Energies,” *The Journal of Chemical Physics*, vol. 123, no. 12, p. 124107, 2005.
45. Perdew, J. P., A. Ruzsinszky, O. A. Vydrov, L. A. Constantin, X. Zhou, and K. Burke, “Restoring the Density-Gradient Expansion for Exchange in Solids and Surfaces,” *Physical Review Letters*, vol. 100, no. 13, 2008.
46. Rappoport, D., N. Crawford, F. Furche, and K. Burke, “Which Functional Should I Choose?”, 2008, <https://dft.uci.edu/pubs/RCFB08.pdf>, accessed in March 2022.
47. Ernzerhof, M., G. E. Scuseria, “Assessment of the Perdew–Burke–Ernzerhof Exchange–Correlation functional,” *The Journal of Chemical Physics*, vol. 110, no. 11, pp. 5029–5036, 1999.

48. Slater, J. C., "Atomic Shielding Constants", *Physical Review*, vol. 36, pp. 57–64, 1930.
49. Boys, S. F., "Electronic Wave Functions. I. A General Method of Calculation for the Stationary States of Any Molecular System", *Proceedings of the Royal Society of London. Series A. Mathematical and Physical Sciences*, vol. 200, no. 1063, pp. 542–554, 1950.
50. Leach, A., *Molecular Modelling Principles and Applications*, Prentice Hall, England, 2001.
51. Marenich, A. V., S. V. Jerome, C. J. Cramer, and D. G. Truhlar, "Charge Model 5: An Extension of Hirshfeld Population Analysis for the Accurate Description of Molecular Interactions in Gaseous and Condensed Phases," *Journal of Chemical Theory and Computation*, vol. 8, no. 2, pp. 527–541, 2012.
52. Mayer, I., "Charge, Bond Order and Valence in the AB Initio SCF Theory," *Chemical Physics Letters*, vol. 97, no. 3, pp. 270–274, 1983.
53. Mayer, I., "Charge, Bond Order and Valence in the AB Initio SCF Theory," *Chemical Physics Letters*, vol. 117, no. 4, p. 396, 1985.
54. Mayer, I., "On Bond Orders and Valences in the AB Initio Quantum Chemical Theory," *International Journal of Quantum Chemistry*, vol. 29, no. 1, pp. 73–84, 1986.
55. Kelly, C. P., C. J. Cramer, D. G. Truhlar, "SM6: A Density Functional Theory Continuum Solvation Model for Calculating Aqueous Solvation Free Energies of Neutrals, Ions, and Solute–Water Clusters," *Journal of Chemical Theory and Computation*, vol. 1, no. 6, pp. 1133–1152, 2005.
56. Bond, G. C., *Heterogeneous Catalysis : Principles and Applications*, Oxford: Clarendon Press, 1974.

57. Thomas, J. M., W.J. Thomas, *Principles and Practice of Heterogeneous Catalysis*, Germany, 2014.
58. Ertl, G., H. Knözinger, F. Schüth, J. Weitkamp, *Handbook of Heterogeneous Catalysis*, Germany, 2008.
59. Védrine, J., “Heterogeneous Catalysis on Metal Oxides,” *Catalysts*, vol. 7, no. 11, p. 341, 2017.
60. Rothenberg, G., *Catalysis: Concepts and Green Applications*, Wiley-VCH, Weinheim, 2008.
61. Bhaduri, S., D. Mukesh, *Homogeneous Catalysis: Mechanisms and Industrial Applications*, John Wiley & Sons, Inc, 2014.
62. Knözinger, H., K. Kochloefl, *Heterogeneous Catalysis and Solid Catalysts*, in: *Ullmann's Encyclopedia of Industrial Chemistry*, Wiley-VCH Verlag GmbH & Co. KGaA, 2000.
63. Kemball, C., D. A. Dowden, M. S. Scurrrell, *Heterogenized Homogeneous Catalysts in: Catalysis*, pp. 215–242, 1978.
64. Barbaro, P., F. Liguori, Heterogenized Homogeneous Catalysts for Fine Chemicals Production, in: B. James, *Catalysis by Metal Complexes*, 2010.
65. Qiao, B., A. Wang, X. Yang, L. F. Allard, Z. Jiang, and Y. Cui, “Single-Atom Catalysis of CO Oxidation Using Pt₁/FeO_x,” *Nature Chemistry*, vol. 3, no. 8, pp. 634–641, 2011.
66. Liu, J., “Catalysis by Supported Single Metal Atoms,” *ACS Catalysis*, vol. 7, no. 1, pp. 34–59, 2016.

67. Liu, J., T. Zhang, “Preface to the Special Issue of the International Symposium on Single-Atom Catalysis (ISSAC-2016),” *Chinese Journal of Catalysis*, vol. 38, no. 9, p. 1431, 2017.
68. Asakura, H. N., N. Ichikuni, Y. Iwasawa, “Structure and Catalytic Combustion Activity of Atomically Dispersed Pt Species at MgO Surface,” *Applied Catalysis A: General*, vol. 188, no. 1–2, pp. 313–324, 1999.
69. Yan, H., H. Cheng, H. Yi, Y. Lin, T. Yao, and C. Wang, “Single-Atom Pd₁/Graphene Catalyst Achieved by Atomic Layer Deposition: Remarkable Performance in Selective Hydrogenation of 1,3-Butadiene,” *Journal of the American Chemical Society*, vol. 137, no. 33, pp. 10484–10487, 2015.
70. Zhao, Z. J., C. Chiu, J. Gong, “Molecular Understandings on the Activation of Light Hydrocarbons over Heterogeneous Catalysts,” *Chemical Science*, vol. 6, no. 8, pp. 4403–4425, 2015.
71. Corma, A., “Heterogeneous Catalysis: Understanding for Designing, and Designing for Applications,” *Angewandte Chemie International Edition*, vol. 55, no. 21, pp. 6112–6113, 2016.
72. Nørskov, K., T. Bligaard, J. Rossmeisl, and C. H. Christensen, “Towards the Computational Design of Solid Catalysts,” *Nature Chemistry*, vol. 1, no. 1, pp. 37–46, 2009.
73. Zhao, Z.C., “Single Mo Atom Supported on Defective Boron Nitride Monolayer as an Efficient Electrocatalyst for Nitrogen Fixation: A Computational Study,” *Journal of the American Chemical Society*, vol. 139, no. 36, pp. 12480–12487, 2017.
74. Mehta, P., P. Barboun, F. A. Herrera, J. Kim, P. Rumbach, and D. B. Go, “Overcoming Ammonia Synthesis Scaling Relations with Plasma-Enabled Catalysis,” *Nature Catalysis*, vol. 1, no. 4, pp. 269–275, 2018.

75. Wei, H., X. Liu, A. Wang, L. Zhang, B. Qiao, and X. Yang, "FeO_x-Supported Platinum Single-Atom and Pseudo-Single-Atom Catalysts for Chemoselective Hydrogenation of Functionalized Nitroarenes," *Nature Communications*, vol. 5, no. 1, 2014.
76. Wang, W. Z., S. Wang, Z. Gao, Z. Luo, and X. Wang, "Atomic-Level Insights in Optimizing Reaction Paths for Hydroformylation Reaction over Rh/CoO Single-Atom Catalyst," *Nature Communications*, vol. 7, no. 1, 2016.
77. Sun, G., Z. J. Zhao, R. Mu, S. Zha, L. Li, and S. Chen, "Breaking the Scaling Relationship via Thermally Stable Pt/Cu Single Atom Alloys for Catalytic Dehydrogenation," *Nature Communications*, vol. 9, no. 1, p. 4454, 2018.
78. Lu, Y., J. Wang, L. Yu, L. Kovarik, X. Zhang, and A. S. Hoffman, "Identification of the Active Complex for CO Oxidation over Single Atom Ir on MgAl₂O₄ Catalysts," *Nature Catalysis*, vol. 2, no. 2, pp. 149–156, 2019.
79. Wang, H., J. X. Liu, L. F. Allard, S. Lee, J. Liu, and H. Li, "Surpassing the Single Atom Catalytic Activity Limit through Paired Pt-O-Pt Ensemble Built from Isolated Pt₁ Atoms," *Nature Communications*, vol. 10, no. 1, 2019.
80. Liu, Y., X. Chai, X. Cai, M. Chen, R. Jin, and W. Ding, "Central Doping of a Foreign Atom into the Silver Cluster for Catalytic Conversion of CO₂ toward C–C Bond Formation," *Angewandte Chemie International Edition*, vol. 57, no. 31, pp. 9775–9779, 2018.
81. Millet, M. M., G. Algara-Siller, S. Wrabetz, A. Mazheika, F. Girgsdies, and D. Teschner, "Ni Single Atom Catalysts for CO₂ Activation," *Journal of the American Chemical Society*, vol. 141, no. 6, pp. 2451–2461, 2019.
82. Yang, J. Liu, S. Lee, B. Zugic, J. Huang, and L. F. Allard, "A Common Single-Site Pt(II)–O(OH)_x– Species Stabilized by Sodium on 'Active' and 'Inert' Supports Catalyzes the Water-Gas Shift Reaction," *Journal of the American Chemical Society*, vol. 137, no. 10, pp. 3470–3473, 2015.

83. Tang, Y., C. Asokan, M. Xu, G. W. Graham, X. Pan, and P. Christopher, "Rh Single Atoms on TiO₂ Dynamically Respond to Reaction Conditions by Adapting Their Site," *Nature Communications*, vol. 10, no. 1, 2019.
84. Rivero-Crespo, A., M. Mon, J. Ferrando-Soria, C. W. Lopes, M. Boronat, and A. Leyva-Pérez, "Confined Pt₁¹⁺ Water Clusters in a MOF Catalyze the Low-Temperature Water-Gas Shift Reaction with both CO₂ Oxygen Atoms Coming from Water," *Angewandte Chemie International Edition*, vol. 57, no. 52, pp. 17094–17099, 2018.
85. Sun, Z., S. Wang, W. Chen, "Metal Single-Atom Catalysts for Selective Hydrogenation of Unsaturated Bonds," *Journal of Materials Chemistry A*, vol. 9, no. 9, pp. 5296–5319, 2021.
86. Crespo-Quesada, F., A. L. Dessimoz, L. Kiwi-Minsker, "Modern Trends in Catalyst and Process Design for Alkyne Hydrogenations," *ACS Catalysis*, vol. 2, no. 8, pp. 1773–1786, 2012.
87. González-Fernández, A., C. Pischetola, L. Kiwi-Minsker, F. Cárdenas-Lizana, "Partial Hydrogenation of 2-Methyl-3-butyn-2-ol over Pd/ZnO: Effect of Reduction Temperature on Alloy Formation and Catalytic Response," *The Journal of Physical Chemistry C*, vol. 124, no. 6, pp. 3681–3691, 2020.
88. Vilé, G., N. Almora-Barrios, S. Mitchell, N. López, and J. Pérez-Ramírez, "From the Lindlar Catalyst to Supported Ligand-Modified Palladium Nanoparticles: Selectivity Patterns and Accessibility Constraints in the Continuous-Flow Three-Phase Hydrogenation of Acetylenic Compounds," *Chemistry - A European Journal*, vol. 20, no. 20, pp. 5926–5937, 2014.

89. Wei, Z., Z. Yao, Q. Zhou, G. Zhuang, X. Zhong, and S. Deng, "Optimizing Alkyne Hydrogenation Performance of Pd on Carbon in Situ Decorated with Oxygen-Deficient TiO₂ by Integrating the Reaction and Diffusion," *ACS Catalysis*, vol. 9, no. 12, pp. 10656–10667, 2019.
90. Fu, Q., "Active Nonmetallic Au and Pt Species on Ceria-Based Water-Gas Shift Catalysts," *Science*, vol. 301, no. 5635, pp. 935–938, 2003.
91. Thomas, J. M., "Tens of Thousands of Atoms Replaced by One," *Nature*, vol. 525, no. 7569, pp. 325–326, 2015.
92. Zhao, X., L. Zhou, W. Zhang, C. Hu, L. Dai, and L. Ren, "Thiol Treatment Creates Selective Palladium Catalysts for Semihydrogenation of Internal Alkynes," *Chem*, vol. 4, no. 5, pp. 1080–1091, 2018.
93. Hagelüken, C., "Markets for The Catalyst Metals Platinum, Palladium and Rhodium", *Metall*, vol. 60, pp. 31-42, 2006.
94. Kielhorn, J., C. Melber, D. Keller, and I. Mangelsdorf, "Palladium – A Review of Exposure and Effects to Human Health," *International Journal of Hygiene and Environmental Health*, vol. 205, no. 6, pp. 417–432, 2002.
95. Thomas, J. M., R. Raja, D. W. Lewis, "Single-Site Heterogeneous Catalysts," *Angewandte Chemie International Edition*, vol. 44, no. 40, pp. 6456–6482, 2005.
96. Li, X. C., X. Lin, Z. J. Zhao, J. Gong, "Theoretical Insights into Single-Atom Catalysts," *Chemical Society Reviews*, vol. 49, no. 22, pp. 8156–8178, 2020.
97. Feng, Q., S. Zhao, Y. Wang, J. Dong, W. Chen, and D. He, "Isolated Single-Atom Pd Sites in Intermetallic Nanostructures: High Catalytic Selectivity for Semihydrogenation of Alkynes," *Journal of the American Chemical Society*, vol. 139, no. 21, pp. 7294–7301, 2017.

98. Rao, D. M., T. Sun, Y. S. Yang, P. Yin, M. Pu, and H. Yan, "Theoretical Study on the Reaction Mechanism and Selectivity of Acetylene Semi-hydrogenation on Ni–Sn Intermetallic Catalysts," *Physical Chemistry Chemical Physics*, vol. 21, no. 3, pp. 1384–1392, 2019.
99. García, J. I. V. Martínez-Merino, J. A. Mayoral, and L. Salvatella, "Density Functional Theory Study of a Lewis Acid Catalyzed Diels–Alder Reaction. The Butadiene + Acrolein Paradigm," *Journal of the American Chemical Society*, vol. 120, no. 10, pp. 2415–2420, 1998.
100. Zhao, Y., D. G. Truhlar, "The M06 Suite of Density Functionals for Main Group Thermochemistry, Thermochemical Kinetics, Noncovalent Interactions, Excited States and Transition Elements: Two New Functionals and Systematic Testing of Four M06-Class Functionals and 12 other Functionals," *Theoretical Chemistry Accounts*, vol. 120, no. 1–3, pp. 215–241, 2007.
101. Walch S. P., C. W. Bauschlicher, "On 3d Bonding in the Transition Metal Trimers: The Electronic Structure of Equilateral Triangle Ca_3 , Sc_3 , Sc^+_3 , And Ti^+_3 ," *The Journal of Chemical Physics*, vol. 83, no. 11, pp. 5735–5742, 1985.
102. Walch, S. P., "On nd Bonding in the Transition Metal Trimers: Comparison of Sc_3 and Y_3 ," *Theoretica Chimica Acta*, vol. 71, no. 6, pp. 449–458, 1987.
103. Mattsson, E., R. Armiento, P. A. Schultz, and T. R. Mattsson, "Nonequivalence of the generalized gradient approximations PBE and PW91," *Physical Review B*, vol. 73, no. 19, 2006.

104. Walker, A. J., A. Harvey, A. Sen, and C. E. H. Dessent, "Performance of M06, M06-2X, and M06-HF Density Functionals for Conformationally Flexible Anionic Clusters: M06 Functionals Perform Better than B3LYP for a Model System with Dispersion and Ionic Hydrogen-Bonding Interactions," *The Journal of Physical Chemistry A*, vol. 117, no. 47, pp. 12590–12600, 2013.
105. Hohenstein, E. G., S. T. Chill, C. D. Sherrill, "Assessment of the Performance of the M05-2X and M06-2X Exchange-Correlation Functionals for Noncovalent Interactions in Biomolecules," *Journal of Chemical Theory and Computation*, vol. 4, no. 12, pp. 1996–2000, 2008.
106. Lemke, H., T. M. Seward, "Thermodynamic Properties of Carbon Dioxide Clusters by M06-2X and Dispersion-Corrected B2PLYP-D Theory," *Chemical Physics Letters*, vol. 573, pp. 19–23, 2013.
107. Paton, R. S., S. Kim, A. G. Ross, S. J. Danishefsky, and K. N. Houk, "Experimental Diels-Alder Reactivities of Cycloalkenones and Cyclic Dienes Explained through Transition State Distortion Energies," *Angewandte Chemie*, vol. 123, no. 44, pp. 10550–10552, 2011.
108. Frisch, G. M. J., W. Trucks, H.B. Schlegel, G.E. Scuseria, M.A. Robb, J.R. Cheeseman, G. Scalmani, V. Barone, B. Mennucci, G.A. Petersson, H. Nakatsuji, M. Caricato, X. Li, H.P. Hratchian, A.F. Izmaylov, J.Bloino, G. Zheng, J.L. Sonnenberg, M.J. Frisch, G.W. Trucks, H.B. Schlegel, G.E. Scuseria, M.A. Robb, G. Cheeseman, J. R., Scalmani, V. Barone, B. Mennucci, H. Petersson, G. A., Nakatsuji, M. Caricato, X. Li, H.P. Hratchian, A.F. Izmaylov, J. Bloino, G. Zheng, J.L. Sonnenberg, K. Hada, M., Ehara, M.; Toyota, R. Fukuda, J. Hasegawa, M. Ishida, T. Nakajima, Y. Honda, O. Kitao, H. Nakai, T. Vreven, J.E. Montgomery, J. A., J. Peralta, F. Ogliaro, M. Bearpark, J.J. Heyd, E. Brothers, K.N. Kudin, R. Staroverov, V. N., Kobayashi, K. Normand, J. Raghavachari, A. Rendell, J.C. Burant, S.S. Iyengar, J. Tomasi, M. Cossi, N. Rega, Dannenberg, J. J., Dapprich, A.D. Daniels, Ö. Farkas, J.B. Foresman, J.V. Ortiz, J. Cioslowski, D.J. Fox, "Gaussian 09, Rev. E.01", *Gaussian Inc.*, 2009.

109. Wang, J., “Structural, Electronic and Magnetic Properties of Scn ($n=2-18$) Clusters from Density Functional Calculations,” *Physical Review B*, vol. 75, no. 15, 2007.
110. Martinez-Macias, C., P. Serna, B. C. Gates, “Isostructural Zeolite-Supported Rhodium and Iridium Complexes: Tuning Catalytic Activity and Selectivity by Ligand Modification,” *ACS Catalysis*, vol. 5, no. 10, pp. 5647–5656, 2015.
111. Feng, Q., S. Zhao, Y. Wang, J. Dong, W. Chen, and D. He, “Isolated Single-Atom Pd Sites in Intermetallic Nanostructures: High Catalytic Selectivity for Semihydrogenation of Alkynes,” *Journal of the American Chemical Society*, vol. 139, no. 21, pp. 7294–7301, 2017.
112. Chen, P. S., J. Lu, B. C. Gates, and D. A. Dixon, “Molecular Models of Site-Isolated Cobalt, Rhodium and Iridium Catalysts Supported on Zeolites: Ligand Bond Dissociation Energies,” *Computational and Theoretical Chemistry*, vol. 1074, pp. 58–72, 2015.
113. Uzun, A., Bhirud, P. W. Kletnieks, J. F. Haw, and B. C. Gates, “A Site-Isolated Iridium Diethylene Complex Supported on Highly Dealuminated Y Zeolite: Synthesis and Characterization,” *The Journal of Physical Chemistry C*, vol. 111, no. 41, pp. 15064–15073, 2007.
114. Helmenstine, A.M., “Bond Dissociation Energy Definition,” 2019, <https://www.thoughtco.com/bond-dissociation-energy-definition-602118>, accessed in April 2022.

APPENDIX A : COPY-RIGHT LIST

The permission for figures which are used in this thesis are presented in Figure A.1, Figure A.2 and Figure A.3.

CCC Marketplace™

This is a License Agreement between Aylin SALTUK ("User") and Copyright Clearance Center, Inc. ("CCC") on behalf of the Rightsholder identified in the order details below. The license consists of the order details, the CCC Terms and Conditions below, and any Rightsholder Terms and Conditions which are included below. All payments must be made in full to CCC in accordance with the CCC Terms and Conditions below.

Order Date	04-Apr-2022	Type of Use	Republish in a thesis/dissertation
Order License ID	1207110-1	Publisher	ROYAL SOCIETY OF CHEMISTRY
ISSN	1463-9076	Portion	Image/photo/illustration

LICENSED CONTENT

Publication Title	Physical chemistry chemical physics : PCCP	Rightsholder	Royal Society of Chemistry
Article Title	Theoretical study on the reaction mechanism and selectivity of acetylene semi-hydrogenation on Ni-Sn intermetallic catalysts.	Publication Type	Journal
Author/Editor	Royal Society of Chemistry (Great Britain), Deutsche Bunsen-Gesellschaft für Physikalische Chemie., Koninklijke Nederlandse Chemische Vereniging., Società chimica italiana.	Start Page	1384
Date	01/01/1999	End Page	1392
Language	English	Issue	3
Country	United Kingdom of Great Britain and Northern Ireland	Volume	21

Figure A.1. The license for Figure 1.1

CCC Marketplace™

This is a License Agreement between Aylin SALTUK ("User") and Copyright Clearance Center, Inc. ("CCC") on behalf of the Rightsholder identified in the order details below. The license consists of the order details, the CCC Terms and Conditions below, and any Rightsholder Terms and Conditions which are included below. All payments must be made in full to CCC in accordance with the CCC Terms and Conditions below.

Order Date	04-Apr-2022	Type of Use	Republish in a thesis/dissertation
Order License ID	1207112-1	Publisher	Royal Society of Chemistry
ISSN	2050-7488	Portion	Image/photo/illustration

LICENSED CONTENT

Publication Title	Journal of materials chemistry. A, Materials for energy and sustainability	Rightsholder	Royal Society of Chemistry
Article Title	Metal single-atom catalysts for selective hydrogenation of unsaturated bonds	Publication Type	Journal
Author/Editor	Royal Society of Chemistry (Great Britain)	Start Page	5296
Date	01/01/2012	End Page	5319
Language	English	Issue	9
Country	United Kingdom of Great Britain and Northern Ireland	Volume	9

Figure A.2. The License for Figure 3.1

CCC | RightsLink®

Home ? Help Email Support Aylin SALTUK

Isolated Single-Atom Pd Sites in Intermetallic Nanostructures: High Catalytic Selectivity for Semihydrogenation of Alkynes

Author: Quanchen Feng, Shu Zhao, Yu Wang, et al
Publication: Journal of the American Chemical Society
Publisher: American Chemical Society
Date: May 1, 2017

ACS Publications
Most Trusted. Most Cited. Most Read.

Copyright © 2017, American Chemical Society

PERMISSION/LICENSE IS GRANTED FOR YOUR ORDER AT NO CHARGE

This type of permission/license, instead of the standard Terms and Conditions, is sent to you because no fee is being charged for your order. Please note the following:

- Permission is granted for your request in both print and electronic formats, and translations.
- If figures and/or tables were requested, they may be adapted or used in part.
- Please print this page for your records and send a copy of it to your publisher/graduate school.
- Appropriate credit for the requested material should be given as follows: "Reprinted (adapted) with permission from (COMPLETE REFERENCE CITATION). Copyright (YEAR) American Chemical Society." Insert appropriate information in place of the capitalized words.
- One-time permission is granted only for the use specified in your RightsLink request. No additional uses are granted (such as derivative works or other editions). For any uses, please submit a new request.

If credit is given to another source for the material you requested from RightsLink, permission must be obtained from that source.

BACK CLOSE WINDOW

© 2022 Copyright - All Rights Reserved | Copyright Clearance Center, Inc. | Privacy statement | Terms and Conditions

Figure A.3. The license for Figure 3.2